AUTOPHAGY
2022, VOL. 18, NO. 3, 540–558
https://doi.org/10.1080/15548627.2021.1936932

Taylor & Francis
Taylor & Francis Group

RESEARCH PAPER

Silencing PEX26 as an unconventional mode to kill drug-resistant cancer cells and forestall drug resistance

Michael S. Dahabieh[a,b,*], Fan Huang[a,*], Christophe Goncalves[a], Raúl Ernesto Flores González[a,b], Sathyen Prabhu[a,b], Alicia Bolt[a], Erminia Di Pietro[c], Elie Khoury[a,b], John Heath[a,b], Zi Yi Xu[a], Joelle Rémy-Sarrazin[a], Koren K. Mann[a,b,d], Alexandre Orthwein[a,b,d], François-Michel Boisvert[e], Nancy Braverman[c], Wilson H. Miller[a,b,d], and Sonia V. del Rincón[a,b,d]

[a]Lady Davis Institute, McGill University, Montréal, Canada; [b]Department of Experimental Medicine, McGill University, Montréal, Canada; [c]Department of Human Genetics and Pediatrics, Research Institute of McGill University Children's Hospital, Montréal, Canada; [d]Department of Oncology, McGill University, Montréal, Canada; [e]Département d'anatomie et de biologie cellulaire, Université de Sherbrooke, Sherbrooke, Canada

ABSTRACT

Promoting the macroautophagy/autophagy-mediated degradation of specific proteins and organelles can potentially be utilized to induce apoptosis in cancer cells or sensitize tumor cells to therapy. To examine this concept, we enriched for autophagosomes from histone deacetylase inhibitor (HDACi)-sensitive U937 lymphoma cells and isogenic HDACi-resistant cells. Mass spectrometry on autophagosome-enriched fractions revealed that HDACi-resistant cells undergo elevated pexophagy, or autophagy of the peroxisome, an organelle that supports tumor growth. To disturb peroxisome homeostasis, we enhanced pexophagy in HDACi-resistant cells via genetic silencing of peroxisome exportomer complex components (*PEX1*, *PEX6*, or *PEX26*). This consequently sensitized resistant cells to HDACi-mediated apoptosis, which was rescued by inhibiting ATM/ataxia-telangiectasia mutated (ATM serine/threonine kinase), a mediator of pexophagy. We subsequently engineered melanoma cells to stably repress *PEX26* using CRISPR interference (CRISPRi). Melanoma cells with repressed *PEX26* expression showed evidence of both increased pexophagy and peroxisomal matrix protein import defects versus single guide scrambled (*sgSCR)* controls. *In vivo* studies showed that *sgPEX26* melanoma xenografts recurred less compared to *sgSCR* xenografts, following the development of resistance to mitogen-activated protein kinase (MAPK)-targeted therapy. Finally, prognostic analysis of publicly available datasets showed that low expression levels of *PEX26, PEX6* and *MTOR*, were significantly associated with prolonged patient survival in lymphoma, lung cancer and melanoma cohorts. Our work highlighted that drugs designed to disrupt peroxisome homeostasis may serve as unconventional therapies to combat therapy resistance in cancer.

Abbreviations: ABCD3/PMP70: ATP binding cassette subfamily D member 3; ACOX1: acyl-CoA oxidase 1; AP: autophagosome; COX: cytochrome c oxidase; CQ: chloroquine; CRISPRi: clustered regularly interspaced short palindromic repeats interference; DLBCL: diffuse large B-cell lymphoma; GO: gene ontology; dCas9: Cas9 endonuclease dead, or dead Cas9; HDACi: histone deacetylase inhibitors; IHC: Immunohistochemistry; LAMP2: lysosomal associated membrane protein 2; LCFAs: long-chain fatty acids; LFQ-MS: label-free quantitation mass spectrometry; LPC: lysophoshatidylcholine; MAP1LC3B/LC3B: microtubule associated protein 1 light chain 3 beta; MTOR: mechanistic target of rapamycin kinase; PBD: peroxisome biogenesis disorders; PTS1: peroxisomal targeting signal 1; ROS: reactive oxygen species; sgRNA: single guide RNA; VLCFAs: very-long chain fatty acids; Vor: vorinostat; WO: wash-off.

ARTICLE HISTORY
Received 12 January 2020
Revised 25 May 2021
Accepted 27 May 2021

KEYWORDS
Apoptosis; autophagy; exportomer; peroxisome; pexophagy

Introduction

Cancer cells tightly regulate the degradation of macromolecules that mediate cell fate. Disturbing the homeostasis of specific macromolecules by promoting their degradation could be utilized to kill cancer cells. Macroautophagy/autophagy is a process whereby damaged macromolecules, including lipids, proteins, and organelles, collectively referred to as cargoes, are initially flagged for degradation via ubiquitination. Cargoes are then encapsulated by an expanding double-membrane vesicle, a phagophore, which forms an autophagosome [1]. These autophagosomes subsequently fuse with lysosomes to degrade cargoes into their building blocks. The autophagy-mediated degradation of specific cargoes in cancer cells may facilitate survival, or conversely, apoptosis [2].

Previous work from our lab exhibits the opposing apoptotic fates of autophagy in an isogenic lymphoma system that models sensitivity and resistance to histone deacetylase inhibitors (HDACi) [3]. Specifically, in HDACi Vorinostat (Vor)-sensitive U937 parental lymphoma cells, we demonstrate that autophagy facilitates apoptosis, while inhibiting autophagy

CONTACT Sonia V. del Rincón sonia.delrincon@mcgill.ca Lady Davis Institute, McGill University
Wilson H. Miller wmiller@ldi.jgh.mcgill.ca Lady Davis Institute, 3755 Chemin de la Côte Ste-Catherine, Room E-504, Montréal, QC H3T 1E2, Canada

*These authors contributed equally to this work
Supplemental data for this article can be accessed here

protects cells from Vor-induced toxicity. Conversely, in the isogenic U937 Vor-resistant cell line, termed B8, blocking autophagy results in apoptosis in the presence of Vor [3].

Autophagy is critical for maintaining cellular homeostasis, and we hypothesized that the contents of the autophagosomes, including proteins and/or organelles, differed in the U937 and B8 cell lines. Previous studies demonstrate that different tumor types can possess variable autophagosome cargoes [4,5]. For instance, analyses of autophagosome cargo proteins from PANC-1 pancreatic cells versus MCF7 breast cancer cells show that more than 60% of identified proteins are exclusive to each cell type [4]. Moreover, different chemical treatments of the same cell type also lead to variations in their autophagosome cargoes. Specifically, when MCF7 cells are incubated with autophagy modulators, such as the MTOR inhibitor rapamycin, the vacuolar type H^+-ATPase inhibitor concanamycin A, or serum starvation, approximately 70% of identified autophagosome cargo proteins in each case are exclusive to their respective conditions [5]. Moreover, recent studies indicate that in addition to proteins, autophagosomes can engulf entire organelles, such as endoplasmic reticula [6,7], mitochondria [8], and peroxisomes [9].

Peroxisomes are highly specialized organelles with vital metabolic functions that include: beta-oxidation of very-long chain fatty acids (VLCFAs) [10], C_{27} to C_{24} bile acid conversion [11], alpha-oxidation of branched-chain fatty acids [12], and the primary steps of plasmalogen synthesis [13]. Considering that cancers may be reliant on alternative metabolic reprogramming for their survival [14], and peroxisomes are essential metabolic organelles, examining the effects of disrupting peroxisome homeostasis in cancer cells is of potential therapeutic interest.

One mode to reduce peroxisome numbers is to promote pexophagy, the autophagy-mediated degradation of peroxisomes. Pexophagy is regulated by the peroxisomal exportomer complex, composed of PEX1, PEX6 and PEX26. On the surface of the peroxisome, PEX1 and PEX6 form a heterohexameric AAA-ATPase, which is anchored to the peroxisomal membrane via PEX26 [15]. The peroxisomal protein PEX5 shuttles peroxisomal targeting signal 1 (PTS1) sequence-containing proteins from the cytosol into the peroxisomal matrix. Upon PEX5-mediated delivery of PTS1-containing proteins into the matrix, the exportomer complex facilitates the recycling of PEX5 from the peroxisomal matrix to the cytosol [16]. When either *PEX1, PEX6*, or *PEX26* are silenced, mono-ubiquitinated PEX5 accumulates on the peroxisomal membrane [17]. An accumulation of peroxisomal membrane-bound ubiquitinated PEX5 in turn recruits the autophagy cargo receptor SQSTM1/p62 (sequestosome 1) [9] or NBR1 [17], to the peroxisomal membrane to cue phagophores to engulf peroxisomes.

A previous study from our group shows that B8 Vor-resistant cells, maintained in Vor, possess elevated peroxisome levels, compared with their isogenic Vor-treated U937 parental counterparts [18]. Additional reports demonstrate that eukaryotic cells regulate superfluous peroxisome levels by triggering pexophagy [19–21]. However, the level at which pexophagy occurs, and whether increasing pexophagy affects cell viability have yet to be established. In this investigation, we first aimed to characterize putative differences in the autophagosome cargo proteins present in the Vor-sensitive (U937) and -resistant (B8) isogenic cells. We found that peroxisome-related proteins were highly abundant within the autophagosome fraction of B8 cells, compared to vehicle- or Vor-treated U937 cells. We speculated that Vor-maintained B8 cells, amid an elevated abundance of peroxisomes [18], utilized pexophagy to maintain peroxisome homeostasis. We then examined the *in vitro* effects of silencing genes encoding the peroxisomal exportomer complex as a method to disrupt peroxisome homeostasis and induce apoptosis in therapy-resistant B8 cells. We next tested the effects of stably repressing *PEX26* using clustered regularly interspaced short palindromic repeats interference (CRISPRi) in melanoma cells for *in vivo* modeling of therapy resistance. Upon targeted therapy of mice, we observed decreased tumor recurrence in *PEX26*-silenced melanoma versus respective controls. Furthermore, bioinformatic analyses of patient tumor samples demonstrated that a transcriptional signature that may reflect elevated pexophagy correlated with increased survival in lymphoma, melanoma, and lung cancer patients. Collectively, this manuscript highlighted that crippling peroxisome homeostasis by silencing *PEX26* can be leveraged to kill therapy-resistant tumors and delay the acquisition of resistance, while transcriptional signatures of pexophagy in cancer patients could serve as valuable predictors in survival outcome.

Results

Enrichment for autophagosomes from HDACi-sensitive and HDACi-resistant isogenic cells using density centrifugation

We previously developed an isogenic U937 lymphoma model system to characterize sensitivity and resistance to the apoptotic effects of Vorinostat (Vor) [3]. Vor-sensitive U937 parental cells and Vor-resistant B8 cells, undergo pro-death and pro-survival autophagy, respectively (Fig. S1A). We hypothesized that different sets and proportions of cargo proteins exist in U937 and B8 autophagosomes (Figure 1A).

To test our hypothesis, we blocked autophagosome-lysosome fusion via chloroquine (CQ) treatment and enriched CQ-treated whole-cell extracts for autophagosomes using a density centrifugation approach, similar to approaches previously used to characterize autophagosome cargo proteins [4,5,22]. As expected, immunoblots demonstrated a time-dependent increase in autophagy markers, SQSTM1/p62, and the cleaved/lipidated form of MAP1LC3B/LC3B (microtubule associated protein 1 light chain 3 beta; LC3B-II) upon CQ treatment. Apoptosis was reduced in U937 cells upon Vor +CQ treatment versus Vor treatment alone as demonstrated by decreased PARP levels (Fig. S1A-D), while CQ treatment increased apoptosis in HDACi-resistant Vor-cultured B8 cells (Fig. S1A and S1E-G). A schematic of the density centrifugation process and downstream analyses is shown in Fig. S2A. Immunoblots for autophagy markers, LAMP2 (lysosomal associated membrane protein 2), SQSTM1, and LC3B-II confirmed that autophagosomes were primarily enriched in the

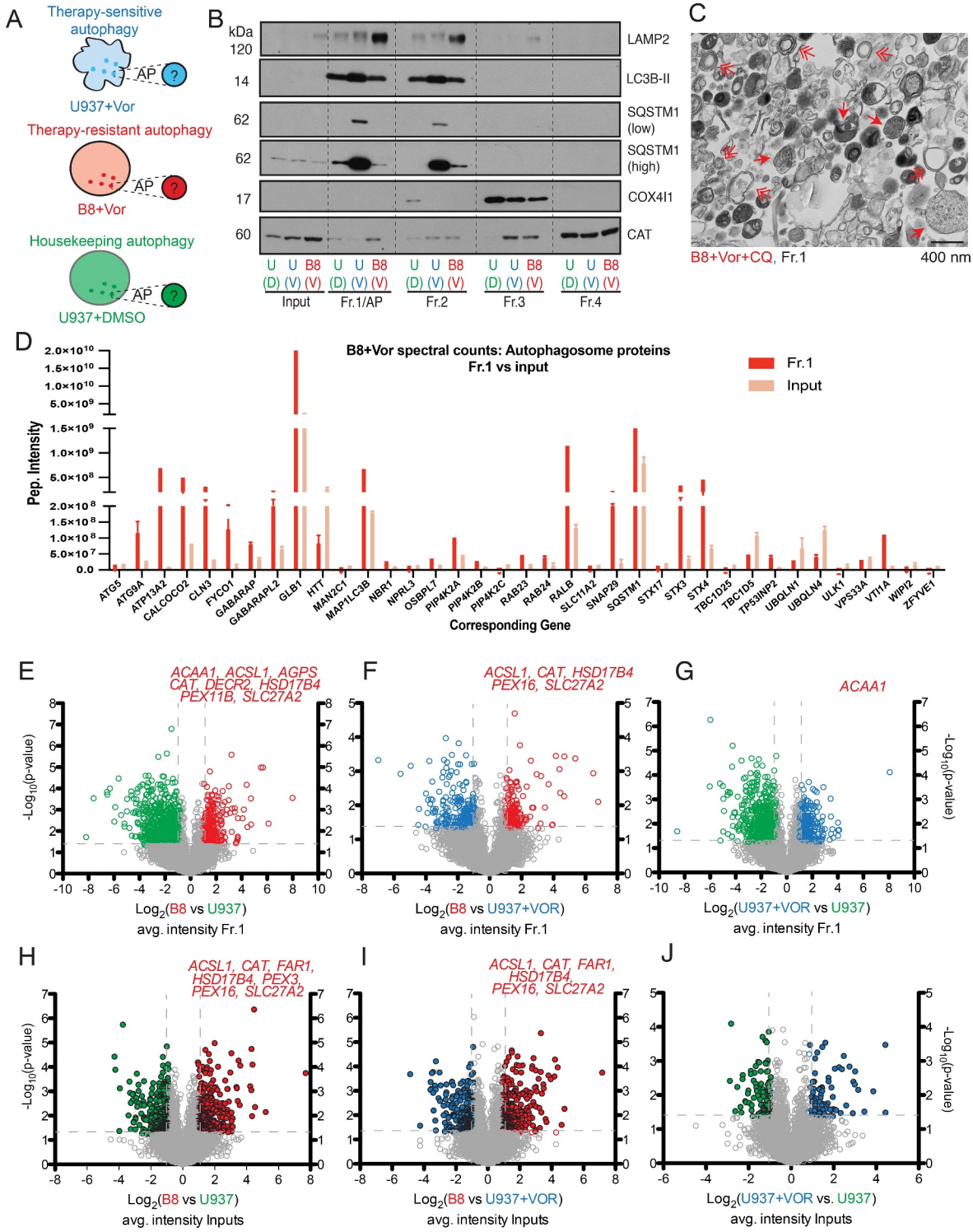

Figure 1. Peroxisomes are elevated in whole-cell and autophagosome fractions upon vorinostat (Vor) treatment. (A) Cell models used: Vor-treated U937 cells (blue), Vor-resistant U937 (B8) cells (red), and DMSO-treated U937 cells (green). Small circles indicate autophagosomes (AP), whereby their putative cargo proteins will be identified via mass spectrometry (MS). (B) Immunoblot of density centrifugation fractions. Lysates from inputs, Fraction 1 (Fr.1-AP enriched), Fr.2, Fr.3 and Fr.4 from chloroquine (CQ)-co-treated cells were immunoblotted for organelle markers: LAMP2 (lysosome), SQSTM1 and LC3B-II (autophagosome), COX4I1 (mitochondria), CAT (peroxisome). Molecular masses (kDa) are indicated on the left. DMSO is represented by (D) and Vor by (V). (C) Electron microscopy of Fr.1. A representative image of Fr.1 extract from CQ-treated B8 (Vor-maintained) cells. Red double arrowheads indicate double-membrane autophagosomes, and red single arrowheads represent granular lysosomes. Scale bar: 400 nm. (D) Intensity counts (vertical axis) of peptides (horizontal axis) corresponding to the listed autophagosome (GO:0005776) genes from Fr.1 and input extracts of Vor-maintained B8 cells. (E–G) Protein MS volcano plots comparing Fr.1 cargos between conditions. (E) B8 vs. U937, (F) B8 vs. U937+ Vor, (G) U937+ Vor vs. U937. Peroxisomal proteins (represented by gene names) are shown for each comparison. (H–J) Protein MS volcano plots comparing inputs (+CQ) of conditions shown in (A). (H) B8 vs. U937, (I) B8 vs. U937+ Vor, (J) U937+ Vor vs. U937. All Vor treatments are 2 μM, and CQ 25 μM.

top fraction of the density centrifugation gradient, termed Fr.1, and partially in Fr.2 (Figure 1B and S2B). The mitochondrial protein COX4I1 (cytochrome c oxidase subunit 4I1), was heavily enriched in Fr.3, whereas the peroxisomal marker CAT (catalase) was most abundant in Fr.4 (Figure 1B and S2B). To further validate the integrity of autophagosomes

from the enrichment procedure, electron microscopy of Fr.1 was performed. Figure 1C shows numerous double-membrane organelles, indicative of autophagosomes (red double arrowheads), while larger single-membrane, granulated structures are indicative of lysosomes (red single arrowheads). Relatively small single-membrane vesicles also appeared in our enrichment, which were likely phagosomes (see Table S1, raw data: PRIDE Archive, PXD013926). The data presented above demonstrated a procedure whereby autophagosomes can be enriched and characterized in subsequent applications.

Peroxisome-related proteins are abundantly detected in the autophagosome-enriched fraction of HDACi-resistant cells

Label-free quantitation mass spectrometry (LFQ-MS) was utilized to assess protein differences between cargoes from enriched autophagosomes (Fr.1) and whole-cell lysates from U937 and B8 cells. We first estimated the fold-enrichment of autophagosomes following our described density centrifugation method (Figure 1B,C and S2A). By utilizing a mass spectrometry (MS) spectral counting method [23], we assessed peptides corresponding to the Gene Ontology (GO) term: autophagosome (GO:0005776) in Fr.1, and respective whole-cell extracts (both samples were treated with CQ). Figure 1D provides a representative peptide intensity plot in Fr.1 and whole-cell extracts (inputs) of B8 cells and exhibits an enrichment in the majority of autophagosome peptides. Similar patterns were observed when comparing Fr.1 vs. input of vehicle and Vor-treated U937 cells (Fig. S2C and S2D). To estimate the fold-enrichment of autophagosomes from the density centrifugation procedure, we plotted individual Fr.1: input peptide intensity ratios corresponding to the autophagosome GO term in vehicle- and Vor-treated U937 cells, along with Vor-cultured B8 cells (Fig. S2E). We observed mean Fr.1:input peptide ratios of 4.5, 4.4, and 3.0 across U937+ DMSO, U937+ Vor, and B8 (Vor), respectively, which indicated an enhanced enrichment of autophagosomes in Fr.1 compared to inputs (Fig. S2E). Top ranked gene ontology (GO)-based molecular functions for Fr.1 have been provided in Fig. S2F.

Peptide signal intensities and inferred protein abundance between Fr.1 of Vor-cultured B8 cells and Fr.1 of vehicle- or Vor-treated U937 cells (Figure 1E–G and Table S1) were next compared. We observed an abundance of peroxisomal proteins in Fr.1 isolated from Vor-maintained B8 cells (Figure 1E, F). For instance, peptides corresponding to peroxisomal protein-encoding-genes *ACAA1, ACSL1, AGPS, CAT, DECR2, HSD17B4, PEX11B* and *SLC27A2*, were increased by two-fold or greater ($p < 0.05$, Student's t-test) in Fr.1 of Vor-maintained B8 versus DMSO-treated U937 cells (Figure 1E). Only *ACAA1* was enriched when comparing Vor-treated U937 to DMSO-treated U937 Fr.1 (Figure 1G). We inferred that peroxisomes may be abundant in B8 autophagosome-enriched fractions, suggesting that Vor-resistant cells used autophagy to engulf peroxisomes, a process known as pexophagy.

B8 cells exhibit increased expression of peroxisome biogenesis proteins, and elevated levels of ABCD3/PMP70 (ATP binding cassette subfamily D member 3) immunofluorescent puncta [18], a surrogate reporter of peroxisome membranes. We were therefore intrigued that the MS revealed evidence of pexophagy in B8, as one might then expect these cells to contain less peroxisomes within the autophagosome-enriched fraction. However, our analysis of LFQ-MS peptide counts on the inputs (i.e., whole-cell extracts) used to enrich for autophagosomes supported that Vor-maintained B8 cells indeed had the highest levels of peroxisomal peptides compared to both vehicle- and Vor-treated U937 extracts (Figure 1H–J and Table S2). As peroxisome homeostasis is tightly regulated [19], our data suggested that B8 cells remove excess, perhaps damaged, peroxisomes by autophagy.

HDACi treatment induces both peroxisome proliferation and pexophagy

We verified our LFQ-MS results using western blot to determine the abundance of peroxisomal proteins in our cell lines. Vor-treated U937 cells contained moderate levels of peroxisomal proteins, compared to Vor-maintained B8 cells, which contained the highest peroxisomal protein levels, while vehicle-treated U937 cells contained the lowest levels (Figure 2A). We next expanded our analysis to examine the levels of additional proteins in peroxisome biology in extracts from U937 cells before and after treatment with Vor, alongside B8 cells maintained or not (wash-off, WO) in Vor. We profiled proteins from the peroxisomal importomer complex (PEX13 and PEX14), peroxisomal protein trafficking proteins (PEX5, PEX7), and members of peroxisomal exportomer complex (PEX1 and PEX6), which exports PEX5 and PEX7 into the lumen [16]. Collectively, PEX5, PEX1, PEX6, and PEX26 orchestrate pexophagy [17]. We observed that Vor-maintained B8 cells had the highest levels of the aforementioned peroxisomal proteins, many of which were repressed after the cells were cultured in the absence of Vor (Figure 2B). Many peroxisomal proteins were increased, in a time-dependent fashion, upon acute Vor treatment of U937 cells, but none reached the elevated levels observed in Vor-maintained B8 cells (Figure 2B).

Our data suggested that the increase in peroxisomes observed in our models was dependent on the presence of the HDAC inhibitor Vor. HDACi treatment results in the net acetylation of histone proteins, which results in transcriptional activation [24]. We therefore assessed whether Vor-induced upregulation of peroxisomes occurred at the mRNA level. The expression of a broad panel of *PEX* mRNAs was detected using qPCR (Figure 2C). We found that the mRNA expression of all *PEX* transcripts, with the exception of *PEX26* and *PEX14*, were significantly upregulated in B8 cells maintained in Vor, compared to the same cells wherein the Vor was washed off for 1 week (Figure 2C). Similar results were obtained in U937 cells acutely treated with Vor, compared to vehicle-treated U937 cells, with *PEX26* and *PEX14* levels not being induced with acute HDACi treatment. We included *FOXO1* and *MAP1LC3B* in our qPCR analysis (Figure 2C), both known

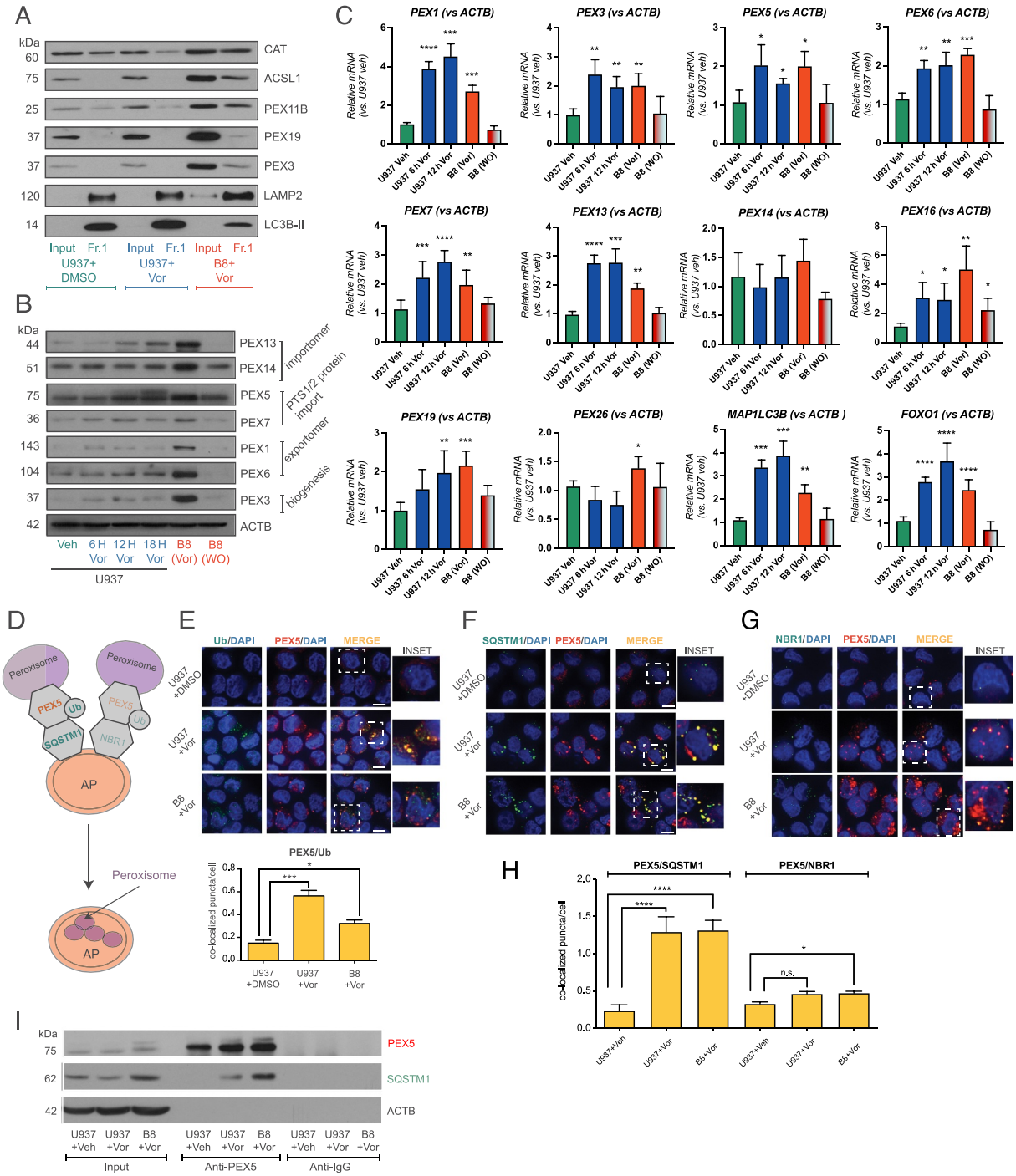

Figure 2. Pexophagy occurs in proportion to whole-cell peroxisome levels. (A) Immunoblot validation of Fr.1 from all conditions, alongside respective whole-cell extracts (inputs). Peroxisomal proteins: CAT, ACSL1, PEX11B, PEX19 and PEX3. LAMP2 and LC3B-II are lysosome and autophagosome protein, respectively. (B) Whole-cell extract peroxisomal protein profile. Shown are acute Vor-treated U937 cells (6,12,18 h), chronically-treated B8 (Vor) and B8 cells washed-off from Vor for one week, referred to as B8 washoff (WO). All samples were treated with CQ. ACTB is a loading control. (C) Relative mRNA expression of *PEX* genes in vehicle and Vor (2 μM)-treated U937 cells, Vor-maintained B8 (B8 [Vor]), and vehicle-cultured B8 (WO) cells. *MAP1LC3B* and *FOXO1* are shown as positive controls for HDACi-induced transcriptional upregulation. All samples were normalized to the housekeeping gene *ACTB*. (D) Schematic of pexophagy. Ubiquitinated PEX5 is attached to the outer surface of the peroxisome and binds the cargo receptors SQSTM1 or NBR1, which facilitates peroxisomal engulfment into an expanding autophagosome (AP). (E) PEX5-Ubiquitin colocalization (+CQ) in vehicle (DMSO)-treated U937, Vor-treated U937, and B8 cells chronically maintained in Vor, with quantitation show below. (F) PEX5 and SQSTM1 colocalization, and (G) PEX5 and NBR1 colocalization (+CQ) in vehicle (DMSO)-treated U937, Vor-treated U937, and B8 cells chronically maintained in Vor. Insets shown for each condition (scale bar for D and E: 10 μm). (H) Number of colocalized puncta per condition (merge) from analyses of (F) PEX5 with SQSTM1, and (G) PEX5 with NBR1 are shown below respective images. (I) Co-immunoprecipitation of PEX5 with SQSTM1 (top), and corresponding inputs (below). All Vor treatments are 2 μM (18 h U937, chronic treatment B8), and CQ 25 μM (18 h).

to be transcriptionally upregulated by HDACi [25]. Thus, Vor enhanced the expression of the majority of the peroxisomal proteins we examined at the transcriptional level.

Peroxisome homeostasis, a balance of peroxisome biogenesis and degradation, is required to maintain appropriate peroxisome number and quality [26]. The abundance of peroxisomal

proteins within Fr.1, and whole-cell extracts of Vor-maintained B8 cells prompted us to hypothesize that pexophagy may be utilized in our model system to maintain peroxisome homeostasis as a consequence of HDACi-induced peroxisome increase (Figure 2C). Molecular signatures of pexophagy include the ubiquitination of PEX5, or peroxisomal membrane proteins, followed by an interaction with the autophagy receptors SQSTM1 [9], and/or NBR1 on the peroxisome surface [27,28] (Figure 2D). To investigate pexophagy in our models of Vor sensitivity and resistance, we first analyzed levels of ubiquitinated PEX5, and PEX5 interacting with SQSTM1 in DMSO- and Vor-treated U937 cells, and Vor-resistant B8 cells. Immunofluorescence analyses showed that PEX5 and ubiquitin colocalized to the greatest extent in cells acutely treated with Vor, with high co-localization in B8 cells also observed, compared to DMSO-treated U937 cells (Figure 2E). We recorded high levels of SQSTM1 co-localized with PEX5 in both Vor-treated U937 and B8 cells maintained in Vor. DMSO-treated U937 cells contained the lowest quantified levels of SQSTM1-PEX5 co-localization (Figure 2F,H). We next tested whether there was any differential contribution for the pexophagy receptor proteins SQSTM1 and NBR1 between our HDACi-sensitive and -resistant models. Immunofluorescence analysis of PEX5 and NBR1 in the presence of Vor demonstrated a less-pronounced co-localization compared to that observed between PEX5-SQSTM1 (Figure 2G,H). We further demonstrated an interaction of SQSTM1 with PEX5 by immunoprecipitation in vehicle and Vor-treated U937 cells, as well as Vor-maintained B8 cells (Figure 2I). However, we were not able to detect a PEX5-NBR1 interaction via immunoprecipitation (Figure 2H and S3A). Thus, in our model systems and in the presence of Vor, PEX5 interacted with SQSTM1, with little to no interaction with NBR1.

Silencing of the exportomer complex in Vor-maintained B8 cells induces pexophagy and increases apoptosis

Having shown that Vor-cultured B8 cells have increased peroxisomes at baseline, relative to U937, and that pexophagy is occurring, we next tested the impact of disrupting peroxisome homeostasis on the survival of drug-resistant B8 cells. PEX1, PEX6, and PEX26 are components of the exportomer complex, which collectively function to suppress pexophagy [17]. Thus, genetic silencing of *PEX1, PEX6*, or *PEX26* is expected to promote pexophagy [17,29,30] (Figure 3A, schematic). We genetically silenced each of the exportomer components *PEX1, PEX6*, and *PEX26* (Figure 3A, right). Upon silencing of *PEX1, PEX6*, or *PEX26*, immunofluorescence analysis revealed an increased co-localization of PEX5 with ubiquitin, and SQSTM1 (Figure 3B,C), both hallmarks of pexophagy [9,17]. Silencing of the exportomer components in B8 cells also resulted in reduced puncta containing ABCD3, which serves as a marker for peroxisome levels (Figure 3D). Finally, we observed that B8 cells underwent apoptosis upon exportomer silencing, compared to the scrambled control siRNA (si*SCR*)-transfected cells (Figure 3E). The latter was consistent with our hypothesis that silencing the exportomer complex promoted pexophagy, thus peroxisome homeostasis was disrupted, and increased apoptosis ensued in Vor-maintained B8 cells.

B8 cells cultured in the absence of Vor (B8-WO) and U937 cells were shown to express similar levels of peroxisomal proteins (Figure 2B). This gave us the opportunity to determine whether the induction of apoptosis upon genetically silencing *PEX26* in B8 cells was dependent on the presence of superfluous peroxisomes that characterize Vor-maintained B8 cells. To address this, we performed a side-by-side comparison of the apoptotic effects of silencing *PEX26* expression in U937 cells, B8 WO cells, and Vor-maintained B8 cells. In B8 WO cells silenced for *PEX26*, we observed no induction of apoptosis compared to its respective *siSCR* control (Fig. S3B and S3C). As expected, *PEX26* silencing increased apoptosis in Vor-maintained B8 cells versus respective scrambled control (Fig. S3B and S3C). Moreover, while an increase in apoptosis was observed in *siPEX26*-transfected U937 cells, apoptosis was not further enhanced upon Vor treatment of *PEX26*-silenced U937, compared to the same *siSCR*-transfected cells treated with Vor (Fig. S3B and S3C). Finally, we directly compared apoptosis levels between *PEX26*- and *PEX3*-silenced B8 cells and observed no significant difference in apoptosis between both approaches (Fig. S3D and S3E). These data demonstrated that disrupting peroxisome homeostasis under conditions where peroxisomes are in excess, as is the case in Vor-maintained B8 cells, resulted in apoptosis. Thus, peroxisomes are suggested to be partial mediators of drug resistance in B8 cells.

ATM is a mediator of apoptosis upon PEX26 *silencing in therapy resistant B8 cells*

We next sought to uncover the mechanism by which *PEX26*-silencing promotes apoptosis. A previous investigation in hepatocellular carcinoma (HepG2) cells demonstrates that ATM signaling drives monoubiquitination of PEX5 at the peroxisomal membrane followed by SQSTM1-PEX5 binding, ultimately leading to pexophagy [9]. We examined whether ATM signaling was implicated in the apoptosis that ensued when we promoted pexophagy via silencing *PEX26* in Vor-cultured B8 cells. We treated B8 cells with two well-described ATM inhibitors termed KU55933 [31] or KU60019 [32], which, as expected, resulted in decreased phosphorylation of both ATM (S1981) and H2AX (S139) (Fig. S4A and S4B). Pharmacological ATM inhibition with either KU55933 or KU60019 rescued the *siPEX26*-induced apoptosis detected in B8 cells (Figure 4A,B and S4C). We next determined the impact of blocking ATM on peroxisome levels by assessing ABCD3 puncta. As anticipated, treatment of B8 cells with *PEX26* siRNA reduced ABCD3 puncta levels versus control cells (Figure 4C). However, treatment with either KU55933 or KU60019 reverted peroxisome levels toward those observed in control scrambled RNA-treated B8 cells (Figure 4C,D). Thus, apoptosis upon *PEX26* silencing in B8 cells was partially attributed to an ATM-mediated decrease in peroxisomes.

Thus far, we have used *PEX26* siRNA to induce pexophagy in our chemo-resistant cells. We next tested whether the chemical inducer of pexophagy, 3-aminotriazole (3-AT) [33], induced apoptosis in B8 cells and whether apoptosis was mediated by ATM. 3-AT treatment induced apoptosis in B8

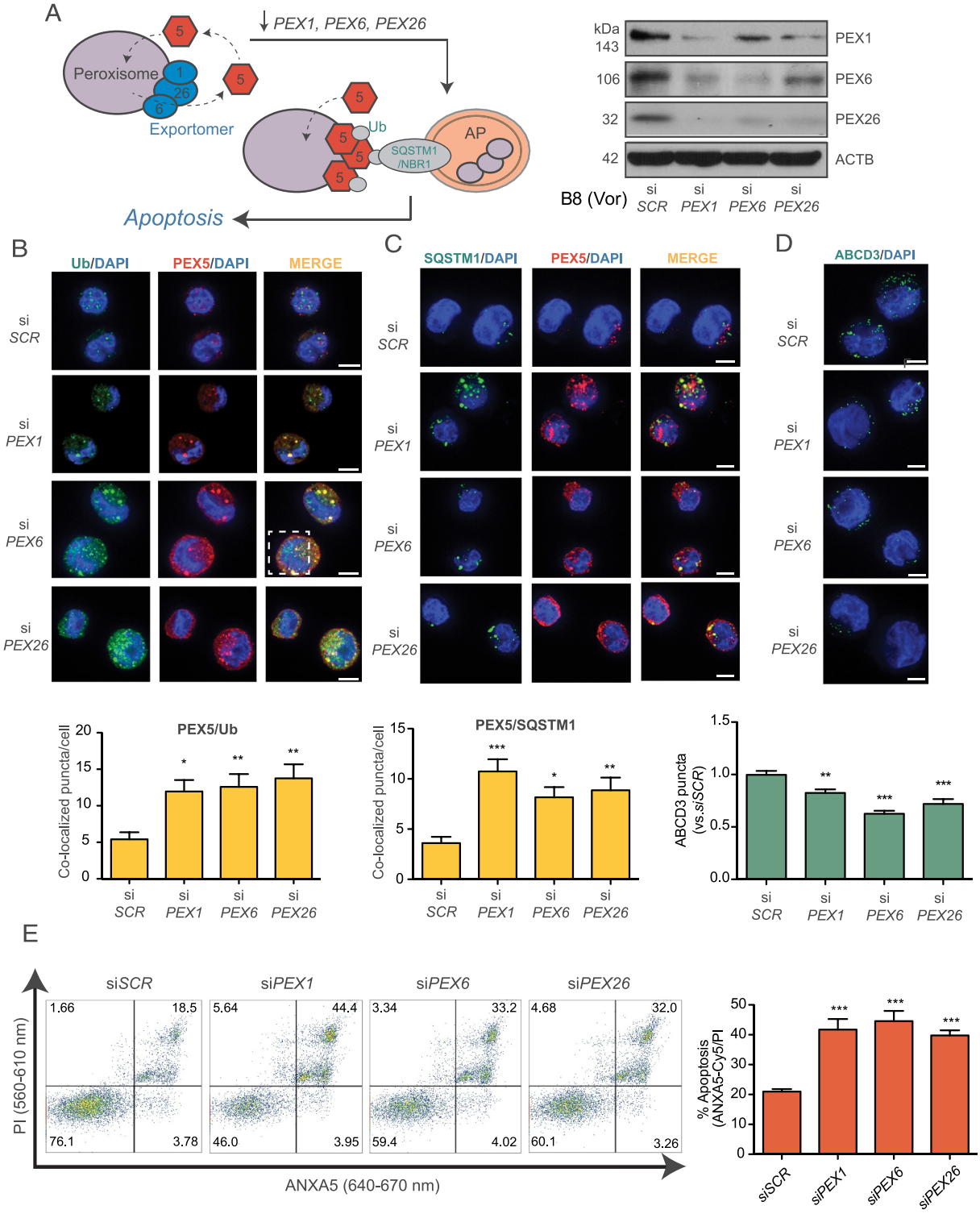

Figure 3. Silencing of the peroxisomal exportomer complex promotes pexophagy and induces apoptosis in Vor-resistant cells. (A, left-schematic) PEX5 (represented by '5') delivers proteins with a peroxisome-targeting signal-1 (PTS1) sequence (not shown) to the peroxisomal matrix. PEX5 is then recycled back to the cytosol via the exportomer complex, consisting of PEX1, PEX6 and PEX26 (blue circles). When the exportomer complex is compromised, PEX5 cannot be efficiently exported to the cytosol. PEX5 then accumulates on the peroxisomal membrane, is ubiquitinated (yellow circles), and interacts with the pexophagy receptor, SQSTM1. The peroxisome then undergoes pexophagy and enters an expanding autophagosome (AP). Peroxisomes within autophagosomes are shown as small purple circles. We hypothesize that pexophagy promotes apoptosis. (A, right) Immunoblots confirming knockdown of PEX1, PEX6, and PEX26 in Vor (2 μM)-maintained B8 (Vor) cells. ACTB is a loading control. (B) Immunofluorescence colocalization in B8 (Vor cells) of ubiquitin with PEX5, and (C) SQSTM1 with PEX5; respective quantifications are shown below. Scale bars for B and C: 7.5 μm. (D) ABCD3 puncta upon silencing of *PEX1, PEX6* and PEX26 in B8 (Vor) cells with quantification shown below. Scale bar: 5 μm. (E, left) Representative flow cytometry scatter plots of ANXA5-Cy5/PI co-stained B8 (Vor) cells. (E, right) Apoptosis measurements 72 h post-transfection, detected by ANXA5-Cy5/PI co-staining. For all statistics: *p < 0.01, **p < 0.001, ***p < 0.0001 (One-way ANOVA, Tukey's test).

cells (Figure 4E), concomitant with a significant reduction in peroxisome levels (Fig. S4D and S4E). Moreover, co-treatment of B8 cells with 3-AT and either ATM inhibitor (KU55933, KU60019) partially rescued apoptosis (Figure 4E). Together our data suggested that pexophagy-induced apoptosis in drug-resistant cells proceeds via an ATM-dependent mechanism.

PEX26 *CRISPRi melanoma cells exhibit decreased peroxisome function and increased pexophagy*

Our findings in B8 cells, a unique model of drug resistance, underscored the importance of assessing the impact of promoting pexophagy in other model systems. To address this, we focused our efforts on BRAF-mutated A375 melanoma cells, which classically exhibit therapy resistance and are amenable to genetic engineering approaches and *in vivo* modeling [34,35]. We stably repressed *PEX26* transcription in A375 cells using CRISPRi (Figure 5A) [36]. Immunoblot profiling of A375 (dCas9 clone A4) *sgPEX26-2* and *sgPEX26-4* cell extracts demonstrated a reduction in the expression of peroxisome exportomer complex proteins, PEX1, PEX6, and PEX26, and the peroxisomal matrix import protein PEX5, compared to A375 *sgSCR* control (Figure 5B). Similar to our B8 model, repression of *PEX26* reduced peroxisomal puncta in *sgPEX26* A375 cells, compared to their *sgSCR* counterparts (Fig. S5A). Importantly, we also observed increased pexophagy in *sgPEX26* versus *sgSCR* cells, as demonstrated by enhanced co-immunoprecipitation of SQSTM1 with PEX5 in *sgPEX26* A375 cells (Figure 5C left, and S5B). Immunoblot densitometry quantitation of SQSTM1 co-immunoprecipitated with PEX5, demonstrated a relatively high ratio of SQSTM1 bound to PEX5 in CQ-treated *sgPEX26* cells versus CQ-treated *scSCR* controls (Figure 5C, right). The densitometry measurements were reflective of input levels for each condition (Figure 5C, left). To complement the co-immunoprecipitation findings, we performed immunofluorescence colocalization analysis of SQSTM1 with PEX5 and observed enhanced SQSTM1-PEX5 colocalization (Figure 5D). To further demonstrate that pexophagy was occurring, we blocked autolysosome formation, and hence peroxisome degradation, using CQ (Figure 5E, top). Here, we observed the highest fold-changes in ABCD3 puncta accumulated upon CQ versus vehicle treatment of *sgPEX26* cells, when compared to CQ and vehicle-treated *sgSCR* cells (Figure 5E bottom, and S5C). The above data demonstrated

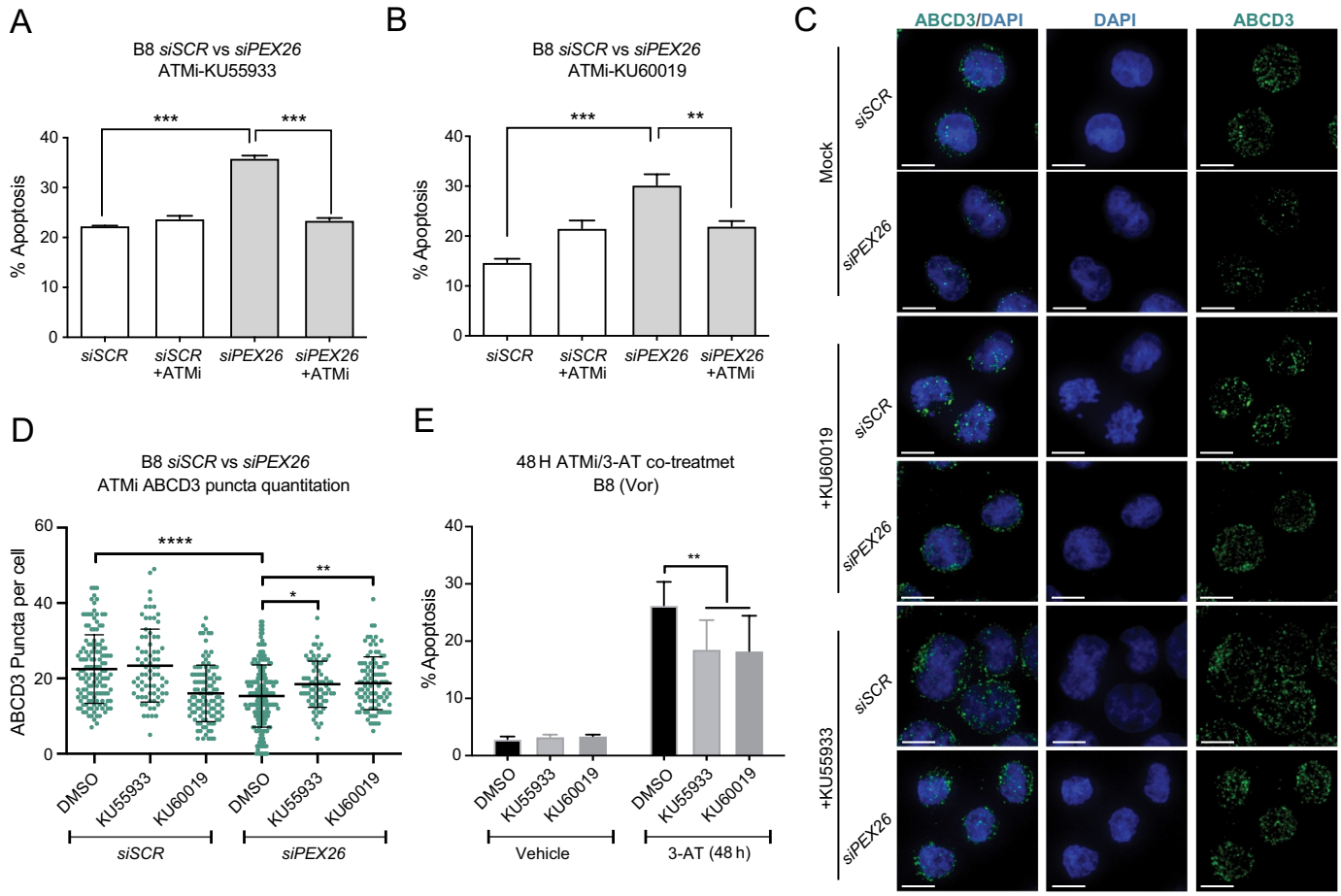

Figure 4. ATM inhibition rescues Vor-resistant lymphoma cells from apoptosis induced by *PEX26* silencing. (A, B) Apoptosis measurements of *siSCR*- or *siPEX26*-transfected B8 cells treated with or without (A) KU55933 and (B) KU60019 for 48 h, detected by ANXA5-Cy5/PI co-staining. (C) Representative IF images of ABCD3 puncta with DAPI nuclear stain (left column), DAPI stain alone (middle), and ABCD3 puncta alone (right). Scale bar: 10 µm. (D) counts of ABCD3 puncta corresponding to (C) in *siSCR*- or *siPEX26*-transfected B8 cells treated with or without KU55933 and KU60019 for 48 h. (E) Apoptosis measurements of B8 cells treated with 3-AT and the ATM inhibitors KU55933 and KU60019 for 48 h. 2 µM of KU55933 and KU60019 were used as indicated. All experiments were repeated 3 times. *p < 0.01, **p < 0.001, ***p < 0.0001 (One-way ANOVA, Tukey's test).

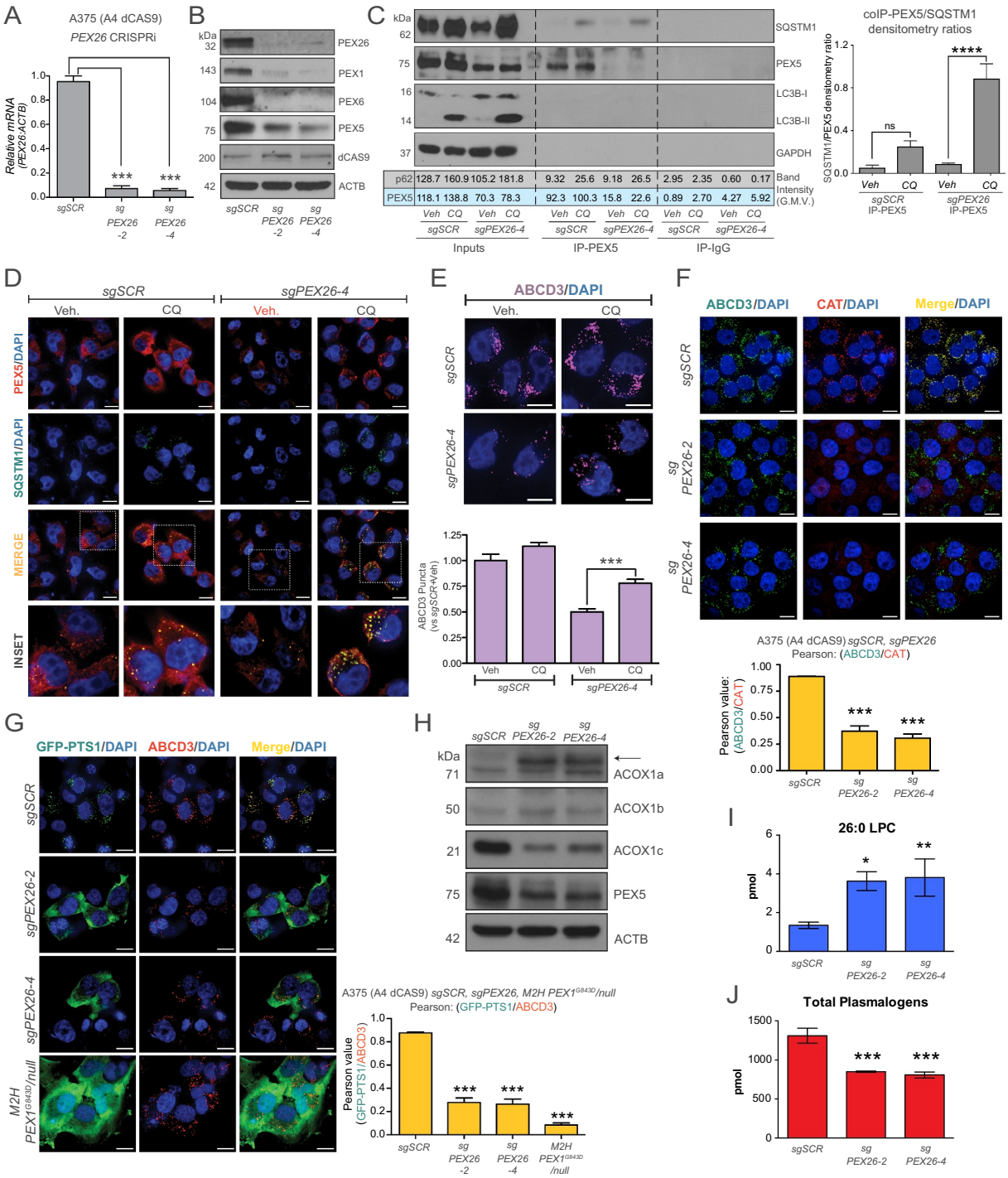

Figure 5. CRISPRi-mediated *PEX26* knockdown decreases peroxisome levels via pexophagy. (A) qPCR analyses of *PEX26* mRNA levels (normalized to *ACTB*) in A375 cell lines stably expressing dCAS9 (clone A4 clone) alongside either *sgSCR, sgPEX26-2* and *sgPEX26-4* RNAs (n = 3, *** p < 0.0001, One-way ANOVA). (B) Immunoblots of dCAS9, PEX1, PEX6, and ACTB in the A375 cell lines presented in panel (A). (C) Immunoblots of PEX5, SQSTM1, (LC3B-II and GAPDH controls) from PEX5 co-immunoprecipitation (co-IP) of *sgSCR* and *sgPEX26-4*, both treated with vehicle (water) or CQ (25 μM, 48 h). Left portion displays immunoblots for inputs (10% of protein from IP), middle portion, PEX5 co-IP. The densitometry (Gray Mean Value, G.M.V.) of SQSTM1 and PEX5 bands are indicated below. Right portion, IgG IP. Right bar graph: densitometry ratio of SQSTM1 and PEX5 from PEX5 co-IP. Results are from three independent experiments, **** p < 0.00001, Two-way ANOVA. (D) Immunofluorescence staining of PEX5, SQSTM1 (DAPI nucleus control) of *sgSCR* and *sgPEX26-4* cells, both treated with vehicle and CQ. Scale bar: 7.5 μm. Insets are shown below respective merge images. (E) Top: Immunofluorescence staining for ABCD3 (purple) of *sgSCR* and *sgPEX26-4* cells, both treated with vehicle and CQ. Scale bar: 7.5 μm. Bottom: ABCD3 puncta quantitation of conditions normalized to *sgSCR* vehicle. n = 3, total of approximately 100 cells counted per condition, *** p < 0.0001, One-way ANOVA. (F) Top: Immunofluorescence staining of ABCD3 (green) and CAT (red), with DAPI (nucleus control, blue) of *sgSCR, sgPEX26-2*, and *sgPEX26-4* cells. Bottom: Pearson values corresponding to co-localization of ABCD3 and CAT (*** p < 0.0001). Fifty cells were analyzed per condition. Scale bar: 7.5 μm. (G) Images: Immunofluorescence staining of GFP-PTS1 (green) and ABCD3 (red), with DAPI (nucleus control, blue) of *sgSCR, sgPEX26-2*, and *sgPEX26-4* cells, and M2H PEX1^{G843D}/null cell line. Bottom right: Pearson values corresponding to co-localization of GFP-PTS1 and ABCD3 (*** p < 0.0001). Fifty cells were analyzed per condition. Scale bar: 7.5 μm. (H) Immunoblot of ACOX1 components "a", "b", and "c", representing the mature 71 kDa polypeptide "a" and peroxisomal proteolytically converted forms "b" and "c" with molecular weights of 50 and 21 kDa. (I) 26:0 LPC measurements (pmol) in *sgSCR, sgPEX26-2*, and *sgPEX26-4* A375 cells, *** p < 0.0001, One-way ANOVA. (J) Total plasmalogen levels (pmol) in *sgSCR, sgPEX26-2*, and *sgPEX26-4* A375 cells, *** p < 0.0001, One-way ANOVA.

that CRISPRi-mediated silencing of *PEX26* in A375 cells provided a reliable model of pexophagy.

We next investigated the integrity of peroxisome-specific functions in the aforementioned model system, as silencing of *PEX26* resulted in defects in the import of peroxisomal matrix proteins (Figure 5F,G). As a consequence of decreased PEX5 levels, hence defective matrix-cytosol shuttling, import of the peroxisomal matrix protein CAT was severely dampened in *sgPEX26* compared to *sgSCR* A375 cells (Figure 5F top, bottom). To further investigate this, we engineered our CRISPRi model system to express a GFP-PTS1 vector, which served as a reporter for generalized PEX5-mediated import of PTS1-bearing proteins [37]. Similar to the CAT-ABCD3 colocalization assay (Figure 5F), we observed decreased GFP-PTS1 import in *sgPEX26* vs. *sgSCR* A375 cells (Figure 5G). Specifically, Pearson values for *sgPEX26* cells were reminiscent of PTS1-ABCD3 colocalization values of the *PEX1* hemizygous peroxisome biogenesis disease (PBD) model cell line, M2H (Figure 5G, bottom right panel).

We next investigated the impact on specialized peroxisome functions in *sgPEX26* versus *sgSCR* A375 cells. Peroxisomes mediate the early steps of plasmalogen synthesis and beta-oxidation of VLCFAs to long-chain fatty acids (LCFAs) [13,38]. ACOX1 (acyl-CoA oxidase 1) facilitates peroxisomal VLCFA beta-oxidation following its trafficking to the peroxisomal matrix via PEX5 [39,40]. ACOX1 is synthesized as a 75-kDa protein (ACOX1a) and is cleaved into 53-kDa (ACOX1b) and 22-kDa (ACOX1c) products within the peroxisome [41]. Thus, relatively high levels of ACOX1a, and low levels of ACOX1b and ACOX1c, versus control cells, can serve as a surrogate marker of peroxisome import and function [41,42]. In *PEX26* CRISPRi cells, we observed decreased cleavage of ACOX1a, consistent with our observations of decreased peroxisomes and hence overall peroxisomal function (Figure 5H and S6A). We finally assessed the function of peroxisomes in *PEX26* CRISPRi A375 cells, versus *sgSCR* controls, by measuring lysophoshatidylcholine (LPC) and plasmalogen levels. We observed an approximately two-fold increase in 26:0 LPC in *sgPEX26* versus *sgSCR* cells (Figure 5I and S6B-H), which suggested defective VLCFA beta-oxidation in *PEX26* CRISPRi cells. Numerous plasmalogen species (Fig. S6I-N), and consequently total plasmalogens (Figure 5J), were markedly reduced in *PEX26* CRISPRi A375 cells. Collectively, these data demonstrated that CRISPRi-mediated repression of *PEX26* compromised import and known peroxisomal functions and served as a suitable tool to interrogate the effects of enhanced pexophagy in a cancer model.

CRISPRi-mediated PEX26 *silencing attenuates tumor relapse in a xenograft melanoma mouse model*

BRAF-mutated A375 cells are sensitive to the BRAF inhibitor vemurafenib and can develop acquired resistance upon chronic exposure to vemurafenib [35]. We next tested the response of *PEX26*-silenced A375 cells (*sgPEX26-4*) to long-term treatment of vemurafenib (Figure 6A). While both the *sgSCR* control cells and the *sgPEX26* cells responded to vemurafenib initially (Figure 6B and S7A, left panel), the *sgSCR* cells developed resistance after two weeks as expected (Figure 6B and S7A). Importantly, the *sgPEX26* cells showed delayed development of vemurafenib resistance and grew significantly slower compared to the *sgSCR* cells (Figure 6B and S7A). This phenotype was rescued when *sgPEX26* cells were maintained in media containing the ATM inhibitor KU55933 (Figure 6B and S7A).

We next examined the *in vivo* effects of stable *PEX26* knockdown on A375 tumor initiation, outgrowth, and response to pharmacological inhibition of $BRAF^{V600E}$ using the vemurafenib analog PLX4720 [35] (Fig. S7B). A375-*sgSCR* or *sgPEX26-4* cells were subcutaneously injected into both flanks of NOD/SCID mice. We observed no significant difference in tumor outgrowth, or time to tumor palpation, between the *sgSCR* and *sgPEX26-4* cohorts of mice fed control chow (Figure 6C). In a separate cohort, mice from each group (*sgSCR* and *sgPEX26-4)* were switched from control chow to chow containing PLX4720 when the tumors reached a volume of approximately 200 mm^3 [43,44] (Figure 6D and S7B). We noted no appreciable difference in initial anti-tumor response to PLX4720 between the *sgSCR* and *sgPEX26-4* cohorts (Figure 6D). At day 30, we observed the maximum reduction in tumor volume in both the *sgSCR* and *sgPEX26-4* groups (Figure 6D). It is well established that resistance to the anti-tumor effects of vemurafenib in mice and patients develops over time [43,45]. Thus, mice were kept on PLX4720 chow to test for the effect of *PEX26* knockdown on the time to tumor relapse, that is, the time to the acquisition of resistance to PLX4720 by measurable tumor volume. We detected the first relapsed melanoma 2 d after robust PLX4720-mediated tumor shrinkage (Figure 6E). Forty-two days following tumor response to PLX4720, approximately 88% (7/8) of the *sgSCR*-derived tumors recurred, while only 44% (4/9) of the *sgPEX26-4*-derived tumors recurred (Figure 6E). Thus, downregulating *PEX26* resulted in delayed disease recurrence following acquired drug resistance. We confirmed that the *sgPEX26-4*-derived tumors expressed approximately three-fold less *PEX26* mRNA than the *sgSCR*-derived tumors, regardless of PLX4720 treatment (Fig. S7C-E). Immunohistochemistry (IHC) staining for PEX26 on tumors harvested from mice bearing *sgSCR* and *sgPEX26-4* tumors was then performed (Figure 6F, images). In tumors from mice fed control chow, positive PEX26 IHC staining was exhibited in approximately 47% and 23% of *sgSCR* and *sgPEX26-4* tumors, respectively (Figure 6F, graph). Similarly, in tumors from mice fed PLX4720 chow, positive PEX26 IHC staining was present in approximately 57% and 38% of *sgSCR* and *sgPEX26-4* tumors, respectively (Figure 6F). Levels of peroxisomal proteins were next investigated from control and *PEX26*-repressed tumors. We observed decreased protein levels of PEX26, PEX1, PEX6 and PEX5, in *sgPEX26-4* tumors from mice fed control chow and PLX4720 chow, compared to their respective *sgSCR* tumors (Figure 6G). We noted an overall increase in p-MAPK1/ERK2-MAPK3/ERK1 expression in the PLX4720-treated tumors (Figure 6G) versus control chow-treated tumors, consistent with the chronic pharmacological inhibition of $BRAF^{V600E}$ resulting in feedback activation of the MAPK1-MAPK3 pathway [46–48]. Collectively, our data demonstrated that stably silencing *PEX26* in A375 cells downregulated the expression of PEX26-associated proteins

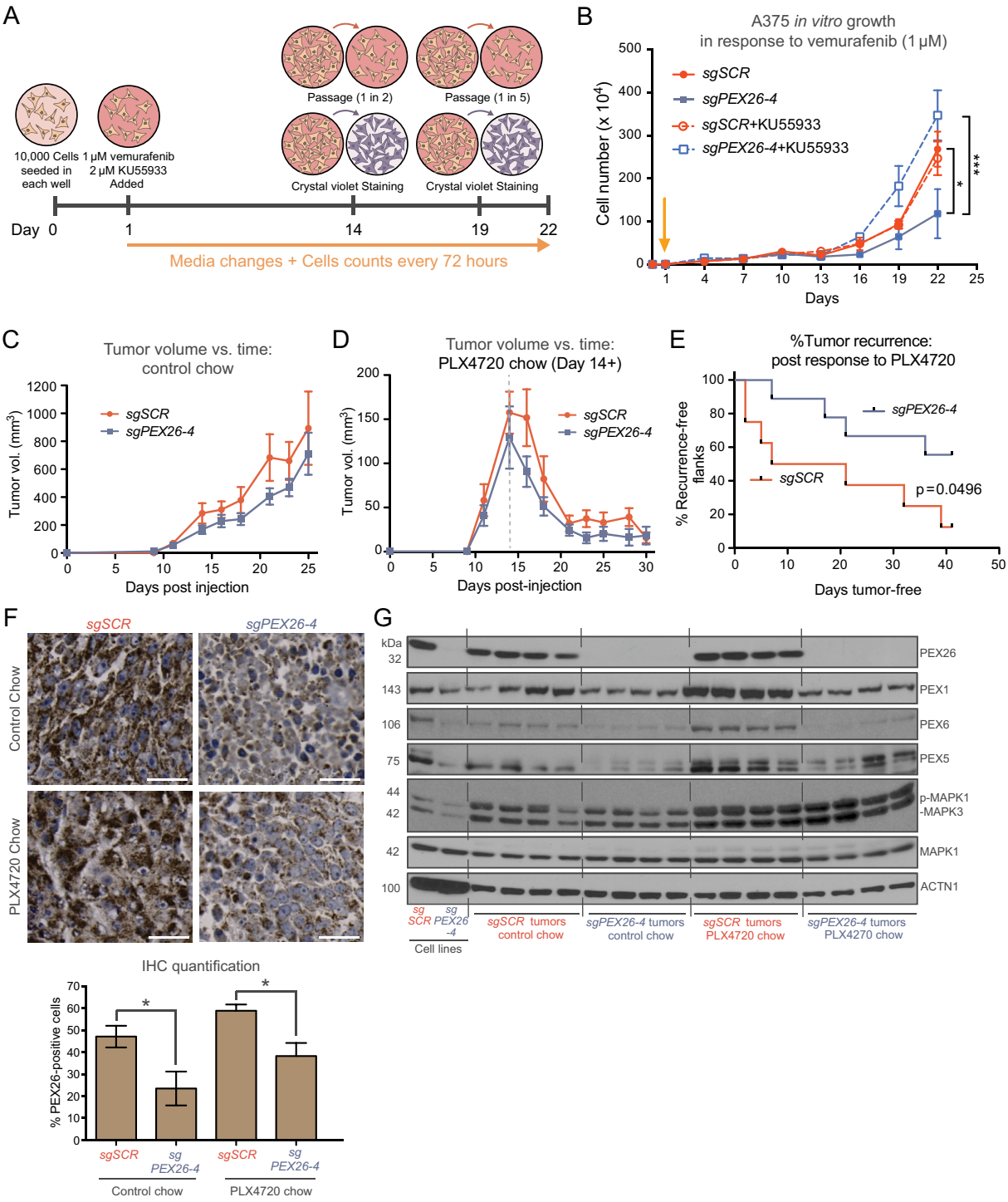

Figure 6. CRISPRi-mediated PEX26 silencing attenuates tumor relapse in a xenograft melanoma mouse model. (A) Schematic of *in vitro* vemurafenib treatment of A375 dCAS9 *sgSCR* and A375 dCAS9 *sgPEX26-4* cells. (B) *in vitro* growth curve of *sgSCR* and *sgPEX26-4* cells in response to 1 μM vemurafenib treatment, maintained in media containing DMSO or 2 μM KU55933. (n = 3, Two-way RM ANOVA with Tukey's multiple comparisons test). (C) Measurements of A375 dCAS9 *sgSCR* and A375 dCAS9 *sgPEX26-4* tumor volume (mm^3) versus days post subcutaneous-injection into 6–10 week old female NOD/SCID female mice (5 mice per group) fed control chow. At day 25, once a critical tumor volume (approximately 1200 mm^3) was reached by at least one mouse, both groups were sacrificed. Tumor volumes were measured every 2–3 d until the endpoint was reached. No significant differences in tumor volume were observed. (D) Tumor volume versus time (days) plot of *sgSCR* and *sgPEX26-4* injected mice. Mice were fed control chow until day 14 (gray dashed vertical line), then chow was switched to the Vemu analog, PLX4720. (E) Recurrence-free survival plot of PLX4720-chow-fed mice injected with A375 dCAS9 *sgSCR* or A375 dCAS9 *sgPEX26-4* cells (p = 0.0496). (F) Top: PEX26 immunohistochemistry (IHC) 3,3′-Diaminobenzidine (DAB) staining of control chow and PLX4720-fed mice, bearing either *sgSCR* or *sgPEX26-4* tumors. Nuclei are stained blue with hematoxylin. Scale bar: 20 μm. Bottom: comparative percentages of PEX26-positive stained (≥ 0.2 mean DAB intensity/cell) *sgSCR* versus *sgPEX26-4* tumors from mice fed control chow (*p = 0.0373, Student's t-test) and PLX4720 chow (*p = 0.0343, Student's t-test). (G) Representative immunoblots from *sgSCR* and *sgPEX26-4* tumors from mice fed control chow, or PLX4720. Shown are PEX26, PEX1, PEX6, and PEX5 (peroxisomal proteins), p-MAPK1-MAPK3 (control for MAPK/ERK reactivation upon chronic PLX4720 treatment), MAPK1, and ACTN1 as a loading control).

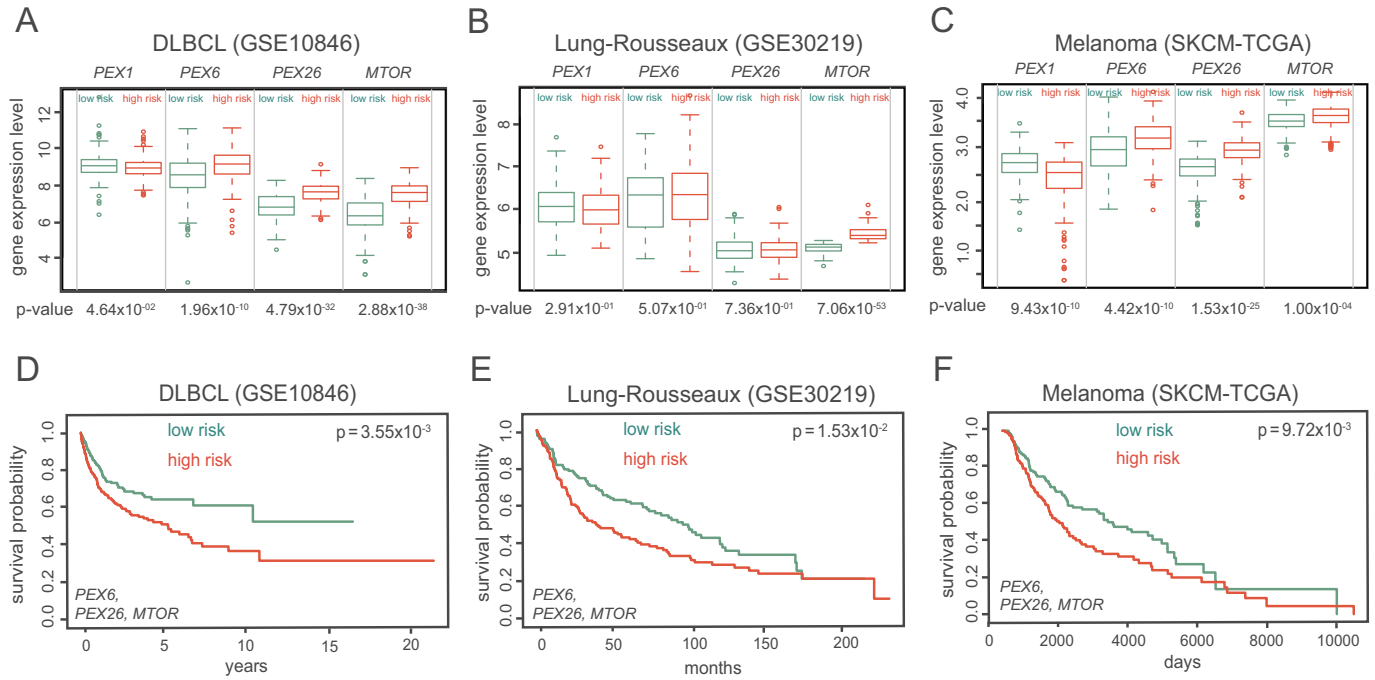

Figure 7. A signature of elevated pexophagy is correlated with increased survival across multiple cancer types. Gene Expression heat maps of *PEX1, PEX6, PEX26* and *MTOR* expression (negative regulators of pexophagy) in (A) DLBCL (GSE10846), (B) Lung cancer (Rousseaux, GSE30219), and (C) melanoma (SKCM-TCGA) cohorts. (D–F) Kaplan-Meier plot (Cox survival) of *PEX6, PEX26*, and *MTOR* expression in DLBCL, lung cancer and melanoma cohorts, respectively. p-values for Kaplan-Meier plots are shown in the top right of each plot.

and forestalled the acquisition of resistance to MAPK-targeted therapy *in vivo*.

A gene expression signature of elevated pexophagy is a prognostic marker for increased overall survival across various cancers

To establish whether our experimental findings had potential clinical relevance, we utilized SurvExpress [49], a biomarker and survival analysis validation tool, to assess whether a putative pexophagy gene signature consisting of *PEX1, PEX6, PEX26* and *MTOR* (mechanistic target of rapamycin kinase), could be used to predict outcomes in tumor cells from cancer patients. The exportomer complex (PEX1, PEX6, PEX26) is a negative regulator of pexophagy (Figures 3–5) [17,29], and *MTOR* is a *bona fide* negative regulator of both autophagy [31] and pexophagy [18]. *PEX1* expression did not differ between high- and low-risk groups in diffuse large B cell lymphoma (DLBCL), but opposed the trends observed for *PEX6, PEX26* and *MTOR* in lung cancer and melanoma cohorts (Figure 7A–C and S8A-C). Exclusion of *PEX1* from Cox-survival analyses did not significantly alter survival probability amongst cohorts (Fig. S8D-F). High expression levels of *PEX6, PEX26* and *MTOR* were associated with high-risk, or decreased survival, in DLBCL, lung cancer and melanoma patients (Figure 7A–C). Subsequent Cox regression for survival analyses using a *PEX6, PEX26* and *MTOR* gene signature were performed on two groups, low-risk (increased probability of survival) or high-risk (decreased probability of survival), of individuals based on gene expression values (Figure 7D–F). In all three cohorts, we observed statistically significant increases in survival in groups with low expression of our gene signature, predicting that increased expression signature of pexophagy-promoting genes in tumors may be attributed to increased patient survival.

In addition to pexophagy, peroxisome levels can be reduced via decreased expression of peroxisome biogenesis genes *PEX3, PEX16* or *PEX19* [18]. Thus, we next examined whether low expression levels of the above genes were associated with significantly increased survival amongst cancer patients. Upon examination of *PEX3, PEX16*, and *PEX19* transcript levels in the same DLBCL, lung cancer, and melanoma cohorts (Figure 7), we observed no significant difference in gene expression between low risk (increased survival) and high risk (decreased survival) groups (Fig. S8G-I). Overall, analyses of publicly available data demonstrated that low expression of negative regulators of pexophagy (*PEX6, PEX26, MTOR*) would predict increased pexophagy, decreased therapy resistance, and increased patient survival (Figure 7).

Discussion

This body of work supported that disrupting peroxisome homeostasis in cancer is a potential unconventional method to overcome or forestall therapy resistance (Figure 8). In this study, pexophagy, and paradoxically peroxisomes, were found to be elevated in HDACi-resistant B8 cells compared to the sensitive line, as identified by our MS analysis of autophagosome-enriched fractions. We discovered that HDACi treatment upregulated peroxisomes at the transcriptional level versus untreated U937 (B8 parental) cells (Figure 2C).

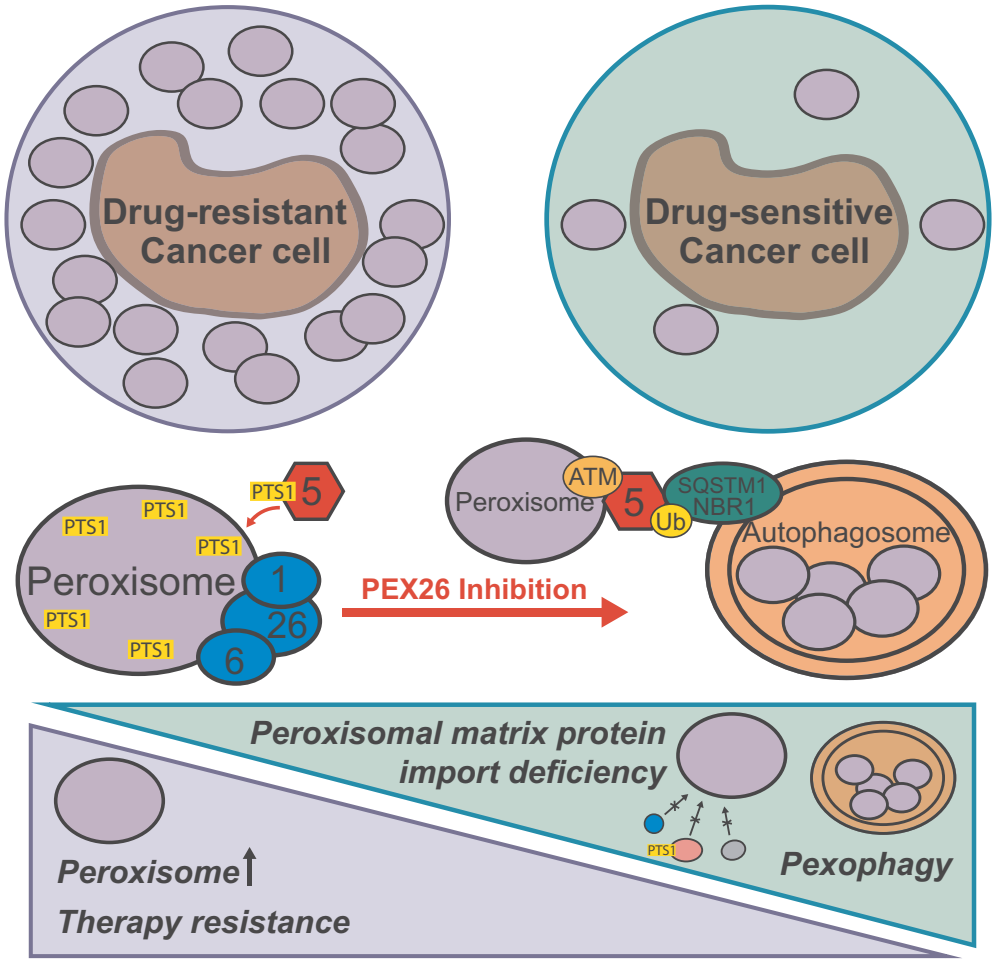

Figure 8. PEX26 silencing mislocalizes peroxisomal matrix proteins, promotes pexophagy and enhances therapy sensitivity. (Top) Drug-resistant cells exhibit increased levels of peroxisomes compared to therapy-sensitive cancer cells. (Middle) When the exportomer complex (PEX1, PEX6, PEX26 – abbreviated with numbered circles) is functional, PEX5 can be recycled back to the cytosol to shuttle PTS1-bearing proteins to the peroxisomal matrix. When the exportomer complex is downregulated via PEX26 silencing or inhibition, ubiquitinated PEX5 interacts with the pexophagy receptor SQSTM1 (or NBR1), which mediates increased engulfment by autophagosomes. ATM localizes PEX5 to the peroxisomal membrane to facilitate pexophagy [9]. (Bottom) Peroxisomes are generally elevated in therapy resistance, while inducing peroxisomal matrix protein import deficiencies and/or pexophagy promotes therapy sensitivity.

However, our data were consistent with a model whereby B8 cells, in an attempt to maintain peroxisome homeostasis, countered the increase in peroxisomes by engaging pexophagy. Our prior works show that HDACi treatment of U937 and B8 cells enhances ROS levels [18,50] and increases autophagosome abundance [3]. Thus, pexophagy may occur upon HDACi treatment as a means of maintaining peroxisome homeostasis, and/or due to HDACi-mediated ROS-mediated macromolecule damage [9,21]. Herein, we showed that disrupting peroxisome homeostasis in B8 cells, via forced pexophagy, triggered an ATM-dependent cell death.

Developing methods to modulate pexophagy carries implications in cancer and PBD. In Vor-maintained B8 lymphoma cells, silencing components of the exportomer complex (*PEX1, PEX6* and *PEX26*), induced hallmarks of pexophagy: PEX5 ubiquitination, PEX5-SQSTM1 binding, and reduced ABCD3 puncta [51]. Importantly, apoptosis was increased by approximately two-fold compared to scrambled controls (Figure 3E). A previous report by the Walker group demonstrates that ATM signaling at the peroxisomal membrane mediates pexophagy in response to elevated levels of H_2O_2. Conversely, ATM-deficient fibroblasts fail to undergo pexophagy upon H_2O_2, treatment compared to control fibroblasts [9]. In HDACi-resistant B8 cells, pharmacologically blocking ATM rescued apoptosis and partially returned peroxisomal puncta toward baseline levels (Figure 4A–C). The importance of ATM in response to therapy when we silenced *PEX26* was further supported in our CRISPRi A375 model system. While we observed an induction of pexophagy upon repressing PEX26 in A375, our data in this model also revealed defects in peroxisomal matrix protein import. It is thus plausible that defective peroxisomal matrix protein shuttling upon *PEX26* silencing, rendered peroxisomes partially dysfunctional and contributed to the observed delay in therapy resistance.

Our *PEX26* CRISPRi A375 model system provided a means of investigating *PEX26* silencing in a stable system (i.e. not relying on transient transfection as in B8). A375 cells acquired resistance to therapy, *in vitro* and *in vivo*, following an initial anti-proliferative response to MAPK-targeted therapy [43,44]. In addition to the induction of pexophagy, stable transcriptional repression of *PEX26* also induced autophagy, as demonstrated by higher levels of LC3B-II in CQ-treated *PEX26*-repressed cells versus CQ-treated *sgSCR* controls

(Figure 5C). In support of *PEX26*-deficient peroxisomes promoting autophagy in our model system, a recent report by Law et al. demonstrates that genetic silencing of *PEX26 (PEX1* and *PEX6)* induces autophagy in HeLa cells [17]. It is plausible that autophagy is upregulated to either facilitate peroxisome degradation, or as a means of survival to cope with potential stresses induced as a result of dampened peroxisome levels. The data we presented in this manuscript from cancer cells indicated that HDACi treatment upregulates peroxisomes, while ATM inhibition partially rescues pexophagy. However, considering that peroxisomes did not completely return to baseline levels upon ATM inhibition suggested that other pathways may mediate peroxisome degradation in our model system. Alternatively, it is plausible that not all membrane-bound PEX5 molecules may be liberated upon ATM blockade, resulting in only a partial rescue of matrix protein import. Nonetheless, it would be of potential interest to the PBD field to test the impact of treatment with HDACi and/or ATMi on reverting peroxisomes toward a functional state.

The mechanism by which pexophagy induction in cancer cells mediates apoptosis and/or attenuates tumor growth could also be postulated based on our current understanding of Mendelian peroxisome biogenesis disorders [52]. A clinical feature of PBD patients, including those with *PEX26* biallelic defects, is decreased cellular levels of plasmalogens [53], essential glycerophospholipids that mediate membrane architecture, undergo ROS quenching [53], and regulate signaling pathways [52]. Our mass spectrometry-based measurements of LPCs in *PEX26*-deficient melanoma cells showed increased 26:0 and 24:0 levels, suggesting defective beta-oxidation. Additionally, we observed decreased plasmalogen levels in *sgPEX26* cells compared to *sgSCR* controls (Figure 5I,J, and S6). AGPS (alkylglycerone phosphate synthase), a peroxisomal enzyme imperative to the initial steps of plasmalogen synthesis, is elevated in aggressive (heightened migratory, invasive and tumorigenic properties) cancer cells, RAS-transformed cells, and primary human tumors [54]. Silencing *AGPS* in aggressive breast cancer lines decreases plasmalogen levels, tumor cell migration/invasion, and tumor growth in xenografts [54]. Future studies will focus on overexpressing plasmalogen-synthesizing enzyme in *PEX26*-deficient melanoma cells to determine the extent to which plasmalogens contribute to tumor proliferation.

Finally, testing whether our pexophagy signature predicted patient outcomes across other cancer types, and recent data highlighting peroxisomes in supporting tumorigenesis and therapy-resistance, may accelerate interest in the development of chemical inhibitors directed against peroxisomal proteins [52]. Inhibiting regulators of transcription of peroxisomal exportomer genes, such as *PEX26*, could be a feasible method of promoting pexophagy. Specifically, in U2OS osteosarcoma cells, PPARGC1A/PGC-1α (PPARG coactivator 1 alpha) controls the transcription of *PEX26, PEX1* and *PEX6*, alongside other *PEX* genes [55]. A small molecule against PPARGC1A (SR-18292) inhibits PPARGC1A-dependent gluconeogenic activity in hepatic cells, ameliorating type 2 diabetes in mouse models [56]. SR-18292 could be tested as a mode of promoting pexophagy, and thus inducing apoptosis in tumor cells. Considering that lipid metabolism is a burgeoning field within tumor biology [57,58], and peroxisomes are specialists at an array of unique lipid-processing pathways [59], specifically promoting pexophagy could illuminate new therapeutic opportunities in cancer.

Materials and methods

Cell culture

U937 cells (ATCC, CRL-1593.2), B8 (Vor-resistant derived from U937), and B8 washoff (WO, 1 week removed from Vor) cells were maintained at cell densities ranging from 300,000–750,000 cells/mL in 75 cm^2 vented flasks (Corning Inc., 430,641 U) with 1640 RPMI (Wisent Bio Products, 350–000-CL), 10% (v:v) FBS (Wisent Bio Products, 080–150) and 0.5% (v:v) penicillin/streptomycin (Wisent Bio Products, 450–200-EL). B8 cells were constantly maintained in 2 μM vorinostat (Cayman Chemical Company, 10,009,929). HEK293FT and the A375 CRISPRi (see below) cells were cultured in DMEM (Wisent Bio Products, 319–016-CL), 10% (v:v) FBS and 0.5% (v:v) penicillin/streptomycin and maintained at 25–75% confluence in 75 cm^2 vented flasks. The patient-derived M2H $PEX1^{G843D}$ (stably expressing GFP-PTS1) was kindly provided by the lab of Dr. Nancy Braverman (Research Institute of McGill University Children's Hospital, Montréal, Canada). M2H cells were cultured in 1640 RPMI (same additives as U937 media) and maintained at 25–75% confluence in 75 cm^2 vented flasks. All cells were incubated at 37°C in 5% CO_2, with a humidity >80% in a Forma™ SteriCycle™ 37°C CO2 incubator (Thermo Fisher Scientific).

Immunoblotting

Immunoblots were performed as previously described [18], with the following primary antibodies (manufacturer, product number, dilution): ACSL1 (Cell Signaling Technology, 9189; 1:1000), ACTB/β-actin (Sigma-Aldrich, A5441; 1:10,000), CAT/catalase (Cell Signaling Technology, 12980; 1:10,000), COX4I1/COX-IV (Abcam, ab14744; 1:500), LAMP2 (Santa Cruz Biotechnology, SC-5571; 1:1000), LC3B-II (Cell Signaling Technology, 3868; 1:1000), SQSTM1/p62 (Santa Cruz Biotechnology, SC-292; 1:1000), PEX1 (BD Biosciences, 61179; 1:1000), PEX3 (Sigma-Aldrich, HPA042830; 1:1000), PEX5 (Proteintech Group, 12545-1-AP; 1:2000), PEX6 (kindly provided by Dr. N. Braverman, 1:2000), PEX7 (Abcam, ab134962; 1:1000), PEX11B (Abcam, ab110004; 1:5000), PEX13 (Proteintech Group, 26649-1-AP; 1:1000), PEX14 (Abcam, ab113286; 1:1000), PEX19 (Proteintech Group, 26649-1-AP; 1:1000).

Immunofluorescence

Immunofluorescence experiments were performed as in the methods section of reference [18]. The following primary antibodies were used (manufacturer, product number; dilution): PEX5 (Proteintech Group, 12545-1-Fr.1; 1:400), ubiquitin (Santa Cruz Biotechnology, SC-8017; 1:100), GFP (Thermo Fisher

Scientific, GF28R; 1:250), SQSTM1/p62 (Santa Cruz Biotechnology, SC-292; 1:100), ABCD3/PMP70 (Abcam, ab211533; 1:200), CAT/catalase (Cell Signaling Technology, 12980; 1:500).

Flow cytometry

All flow cytometry experiments were conducted on the LSRFortessa (BD Biosciences). Cells were initially centrifuged at 300 xg for 5 min, washed twice in 1X PBS (Wisent, 311–425-CL), with 5-min spins at 300 xg. For apoptosis detection 300,000 cells were co-stained with 1.5 µL of ANXA5/annexin V-Cy5 (BD Biosciences, 559933) and 0.25 µg/mL of PI (BD Biosciences, 51–66211E), in 1X binding buffer (BD Biosciences, 556454) per tube.

ATM phosphorylation assay

Cells were incubated with ATMi, KU55933 (Selleck Chemicals LLC, S1092) or KU60019 (Selleck Chemicals LLC, S1570), for 1 h prior to treatment with neocarzinostatin (Sigma-Aldrich, N9162; 0.5 ug/mL) for 1 h. Cells were washed and fresh media was replaced, allowing the cells to initiate response to genotoxic stress. Cell were collected 2 h post treatment via trypsinization and washed twice in PBS. Cells were fixed at room temperature (RT) in 2% PFA-PBS, followed by two washes in PBS, and then permeabilized via the addition of 95% ethanol dropwise, under agitation, to a final concentration of 70% and stored at −20°C until use. Cells were centrifuged at 900 g and washed once with cold PBS and once with PBS containing 1% (w:v) BSA (Sigma-Aldrich, A7906) and 0.05% (v:v) Tween 20 (Bio-Rad Laboratories, 1610781) (PBSA-T) at RT. Cells were incubated in PBSA-T with both anti-p-H2AX(S139) (EMD Millipore, JBW301; 1:1000) and anti-p-ATM(S1981) (Cell Signaling Technology, D25E5; 1:1000) for 1 h at room temperature. Cells were washed with PBS, and incubated with secondary antibodies (goat anti-rat Alexa Fluor 488 [A-11070]; goat anti-mouse Alexa Fluor 647 [A-21237]; Thermo Fisher Scientific) for 1 h at RT. Cells were washed with PBS, followed by data collection (minimum 10,000 events) on a BD Fortessa (Becton Dickinson).

siRNA transfection

Transfections were performed as previously described [18]. Cells were treated for 48 h after which knockdowns were validated and downstream experiments performed. The following siRNAs were used: All-stars negative control siRNA (siSCR, Qiagen, proprietary sequence).

PEX1 Duplex (IDT):

5′-rCrUrArGrArGrArUrUrUrUrArCrArGrUrArCrUrUrGrUrGGA-3′

5′-rUrCrCrArCrArArGrUrArCrUrGrUrArArArArUrCrUrCrUrArGrCrC-3′

PEX6 Duplex (IDT):

5′-rCrUrArCrGrCrGrUrUrCrUrArArGrUrCrGrGrArUrCrArCAC-3′

5′rGrUrGrUrGrArUrGrGrCrArCrUrUrArGrArArCrGrC-rGrUrArGrCrU-3′

PEX26 Duplex (IDT):

5′- rCrUrCrArCrUrGrGrArUrArArCrArUrCrUrArArArUrUrCTT-3′

5′-rArArGrArArUrUrUrArGrArUrGrUrUrArUrCrCrArGrUrGrArGrCrC-3′

In-gel digestion and LC-MS/MS

For MS measurements, whole cell extracts (inputs), and density centrifugation samples were lysed in AMPK buffer (see above), then subjected to in-gel digestion and LC MS/MS as described in reference [60].

Density centrifugation

U937 and B8 cells were each seeded at 500,000 cells/mL in 600 mL of 1640 RPMI with 10% (v:v) FBS, 0.5% (v:v) pen/strep. U937 cells were co-treated with either DMSO/25 µM CQ (Cayman Chemical Company, 14,194) for 18 h (U937), 2 µM Vor/25 µM CQ (U937+ Vor), or in the case of B8 cells maintained in 2 µM Vor and treated with 25 µM CQ for 18 h. Cells were harvested via centrifugation at 100 xg for 5 min, media were aspirated, and pellets were washed twice with 1X PBS. Pellets were then resuspended in 0.5 mL homogenization (HM) buffer (0.25 M NaCl, 1 mM EDTA (Sigma-Aldrich, EDS-1 KG) 20 mM HEPES (Sigma-Aldrich, H4034)-NaOH, pH 7.4, + 1 tablet of cOmplete^{TM}, Mini, EDTA-free protease inhibitor cocktail per 10 mL buffer (Roche, 4,693,159,001), and sheared through a 26-gauge syringe until intact cells were no longer visible under a hemocytometer. Sheared cells were then further diluted with HM buffer and Nycodenz (Sigma-Aldrich, D2158), to a final concentration of 52% and volume of 2.4 mL, which was loaded on the bottom of a 13.2 mL ultracentrifuge tube. 3 mL of 26% Nycodenz, followed by 2 mL of 24%, 2.5 mL of 20%, and 2.5 mL of 20% were successively added overtop each other to form a discontinuous gradient. Samples were then spun in a Beckman Coulter Optima XPN-80 ultracentrifuge at 104,613 xg for 3 h, and the interface separating the 15 and 20% layers was isolated and spun at 21,000 xg in a table-top centrifuge. Other interfaces were also collected and analyzed via western blot. Following microcentrifugation, samples were washed twice with 1X PBS + protease inhibitor cocktail, and processed for downstream applications (western blot, mass spectrometry, electron microscopy).

Electron microscopy

For electron microscopy (EM) processing, samples corresponding to Fr.1 were pelleted according to the final step of the Nycodenz density centrifugation protocol, washed 3X in 1X PBS to remove excess Nycodenz, then fixed in 2% formaldehyde and 2.5% glutaraldehyde in 0.1 M sodium cacodylate buffer, pH 7.4. Samples were stored at 4°C, then processed via initially washing 3X in cacodylate buffer, then incubating in 1% osmium tetroxide-1.5% potassium ferrocyanide (in H_2O) for 1 h at RT in the dark. Pellets were then washed in H_2

O (or in malelate buffer pH 5.15) 3–4x 1% uranyl acetate in H_2O (or in maleate buffer) for 30 min – 1 h, followed by a wash in H_2O 3x with subsequent dehydration: 70% EtOH 15 min, 90% EtOH 15 min, 100% EtOH 2 × 15 min. Samples were then incubated with propyleneoxide (Sigma-Aldrich, 82,320) for 1 h followed by Infiltration: Epon-epoxy embedding medium (Sigma-Aldrich, 45,345) mixed 1:1 with propyleneoxide at RT 2–3 h. An embedding mold filled with freshly mixed Epon was prepared, whereby samples were placed and placed in an oven for polymerization for 24–48 h at 60°C.

In vitro *growth curve*

A375 *sgSCR* and *sgPEX26-4* cells were seeded at 10,000 cells/well in 6-well plates on day 0. The next day, cells were treated with 1 μM vemurafenib (Plexxikon, Berkeley, CA) and 2 μM KU55933 or corresponding control as indicated. Cells were manually counted from day 1 and every 3 d. When confluent, cells were trypsinized and subsequently seeded in a new plate as indicated in Figure 6A.

Immunoprecipitation (IP)

U937 and B8 cells were co-cultured under the same conditions used for autophagosome enrichment described in the density centrifugation section above, at a density of 500,000 cells/mL in 30 mL of respective media for each PEX5 or IgG IP. For CRISPRi A375 cell lines, 1×10^6 cells were initially seeded into 15 mL of respective media (see cell culture section of methods for details) in a 75-cm^2 flask, and vehicle (H_2O) or 25 μM CQ was added 48 h post-seeding. Cells were harvested 24 h later. For U937, B8, and A375 PEX5 and SQSTM1 co-immunoprecipitations, cells were harvested from 75 cm^2 flasks by pipetting (U937, B8), or trypsinization (A375), and washed twice in sterile 1X Dulbecco's PBS (Multicell, 311–425 CL). Cells were next lysed on ice for 15 min with 1X CST lysis buffer (Cell Signaling Technology, 9803), 0.384% v:v protease inhibitor (Sigma-Aldrich, P8340), 0.384% phosphatase inhibitor cocktail 2 (Sigma-Aldrich, P5726), 1% v:v phosphatase inhibitor cocktail 3 (Sigma-Aldrich, P0044). Extracts were then centrifuged at 10,000 xg for 10 min and the supernatant was transferred to fresh 1.5-mL tubes. Lysates were quantitated and diluted to 1 mg/mL in 1X CST buffer with inhibitors. All lysates were then pre-cleared with 30 μL of Protein G Dynabeads™ (Thermo Fisher Scientific, 1004D) and incubated on a nutator for 1 h at 4°C. Lysates with beads were then spun at 1500 xg for 2 min, placed over a magnetic stand, and supernatants were transferred to new 1.5-mL tubes. For PEX5 immunoprecipitations, 2.5 μg of PEX5 antibody (Proteintech Group, 12,545-1-AP) was added to sample tubes containing 1 mg of protein extract in 1 mL lysis buffer, while 2.5 μg of IgG control antibody (Proteintech Group, 3000-0-AP) was added to separate tubes containing 1 mg of respective protein extracts in 1 mL lysis buffer. Samples were then incubated overnight (16–18 h) on a nutator at 4°C. The following day, 30 μL of Protein G Dynabeads were added to all samples and incubated for 1 h on a nutator at 4°C. Samples were quick spun at 1500 xg for 1 min and placed on a magnetic stand for 2 min. The supernatant was gently aspirated, and beads were washed by taking samples off the magnetic stand and pipetting up and down with cold 1X CST buffer (with inhibitors) over ice. Samples were then placed back on the magnetic stand, and the wash procedure was repeated two more times. After the last wash, samples were kept on the magnetic stand, liquid was aspirated, and 120 μL of 1X Blue Loading Buffer Pack cocktail (Cell Signaling Technology, 7722) was added to all samples, tubes were vortexed, and incubated at 95°C for 8 min. Protein extracts were separated from magnetic beads and loaded on acrylamide gels for downstream immunoblot analysis.

Densitometry measurements

Intensity of each band (Gray Mean Value) was quantified using ImageJ (ROI tool), background value was measured at a blank region of the same film and was subsequently subtracted from the gray mean value of each band.

Mass-spectrometry (MS) analyses

All MS data presented in this manuscript were uploaded onto Proteomics IDEntifications (PRIDE) database (PXD013926) Using the label-free quantification function from MaxQuant software (version 1.4.1.2), output data from nine autophagosome enrichment experiments (U937 DMSO/CQ, U937 + Vor/CQ, B8+ Vor/CQ, n = 3), and nine respective whole cell extract inputs (U937 DMSO/CQ, U937+ Vor/CQ, B8 + Vor/CQ, n = 3) was arranged into a single file containing peptide identities, counts, intensities, etc (see attached MS data). With Perseus software (version 1.6.7.0, MaxQuant platform), rows containing "reverse" and "contaminant" were initially removed, followed by rows, which contained a zero-intensity value for peptides across all rows. We first examined (Log_2) relative peptide intensities from each Fr.1 based on the following criteria: (1) scored a p-value of 0.05 or lower upon a Student's t-test comparison between biological triplicates of two conditions (e.g. n = 3, B8+ Vor/CQ vs. n = 3, U937 + DMSO/CQ), (2) corresponding peptide intensities were two-fold greater with respect to the conditions under comparison, and (3) identified protein identities overlapped between two separate t-tests (e.g. common B8 proteins between B8 vs U937 and B8 vs U937+ Vor). The same approach was followed for analysis of inputs. For selectivity analysis (B8+ Vor/CQ Fr.1 vs. B8+ Vor/CQ input), a Student's t-test of respective biological triplicates was performed and analyzed based on a minimum two-fold enrichment and p-value of 0.05 or lower.

RNA expression analyses

A "negative regulation of pexophagy" signature was first assembled consisting of *PEX1, PEX6, PEX26*, and *MTOR*. This signature was analyzed in DLBCL (GSE10846), lung cancer (Rousseaux, GSE30219), and melanoma (SKCM-TCGA) data sets using SurvExpress, an online tool for biomarker validation in cancer gene expression [49]. Original (Quantile-Normalized) data sets were censored based on days to death and last follow up and divided into two risk

groups: "high risk" and "low risk" based on prognostic index rank from the Cox model. Heat maps of each gene were generated based on risk groups, with gene expression values plotted with respect to each individual (within a risk group). Histograms were embedded within scale bars to display the number of individuals with a given expression value. P-values were also displayed which are based on relative gene expression levels between "high risk" and "low risk" groups. A Kaplan-Meier curve was plotted based on aggregation of individual gene expression and days to death/last follow up within the data set. An aggregated p-value was also displayed for each curve. *PEX1* expression opposed that of *PEX6, PEX26*, and *MTOR*, we excluded this from downstream Kaplan-Meier analyses, as *PEX1* would further decrease the overall p-value of the Kaplan-Meier curve, and misrepresent the survival analyses.

qPCR

The methodology for qPCR was followed as previously described [18]. All primer sequences are found in Table S4.

PEX26 CRISPRi cell line generation

2 million HEK293FT cells were seeded onto 10 cm dishes and lentiviral particles were generated housing the pHR-SFFV-dCas9-BFP-KRAB plasmid (Addgene: 46,911, depositing labs: Stanley Qi, Jonathan Weissman) [61]. 2 mL of lentiviral particles were transduced overtop 500,000 A375 cells in a 10 cm dish (final volume 10 mL). Four days after transduction, BFP-positive cells were single-cell sorted (FACSAria Fusion cell sorter) in a 96-well dish (Corning Inc., 3598) containing A375 culture media. Two separate clones, termed A4 and F3, from the 96-well dish were utilized for downstream experiments following expansion and validation by positive immunoblot for dCAS9. *PEX26* guide RNAs, termed *PEX26-2*, and *PEX26-4* were obtained from Human Genome-wide CRISPRa-v2 Libraries (Addgene, 83978, 1000000091, depositing lab: Jonathan Weissman), were cloned into the pRNU6-sgRNA EF1Alpha-puro-T2A-BFP (Addgene, 60955, depositing lab: Jonathan Weissman) puromycin-resistant vector, then generated according to methods presented in [62]. Respectively, *PEX26-2* and *PEX26-4 and scramble* sgRNAs were:

5′ GAAAGACTCACCTCGCCTCC 3′,
5′ GGCTAGGGCCAGGTATTCCA 3′
5′ GTCCACCCTTATCTAGGCTA 3′.

Following validation of correct cloning by Sanger Sequencing, plasmids were incorporated into lentiviral particles and transduced overtop 500,000 A4 and F3 dCAS9-expressing cells. Following selection in 2 μg/mL puromycin (Sigma-Aldrich, P9620), A4 and F3 cells expressing either *sgSCR, sgPEX26-2* and *sgPEX26-4* were generated.

Mouse experiments

All animal experiments complied with McGill University's guidelines on animal care and were conducted in pathogen-free conditions. Twenty female nonobese diabetic (NOD)/severe combined immunodeficiency (SCID) mice aged 6–10 weeks old were randomized and separated into two groups of ten. One group was subcutaneously injected in both flanks with 1 million A375 dCAS9 *sgSCR*-expressing cells, and the other group with 1 million A375 dCAS9 *sgPEX26-4*-expressing cells. All mice were fed control irradiated chow (Research diet, AIN-76A) until day 14, where half the mice from each group were fed chow containing PLX4720. Tumor volumes were measured two to three times weekly, and volumes were calculated according to the formula: $V = (W^2 \times L)/2$, where W = width (mm), and L = length (mm), until the volume endpoint of approximately 1200 mm^3 was reached. For Recurrence-Free Survival plots, tumors that measured ≤ 40 mm^3 following PLX4720 chow administration were considered ablated, as measurement within this range were subject to high variability. For subsequent RNA (qPCR) and immunoblot experiments, tumors were pulverized with a mortar and pestle under liquid nitrogen and further processed according to qPCR and immunoblotting techniques in the respective aforementioned methods sections.

Immunohistochemistry staining

Tumors were harvested, fixed in 10% formalin for 24 h at 4°C, then exchanged for 70% ethanol (EtOH) until embedding. Slides with tissues were deparaffinized and hydrated by the following steps at room temperature (RT): 3 incubations with xylene for 5 min each, 2 incubations in 100% EtOH, 1 incubation in 95% EtOH, 1 incubation in 70% EtOH, running tap water for 5 min, followed by submersion in ddH_2O for 2 min. Tissue slides were then submerged in a container containing 1X TE (10 mM Tris-Cl, pH 8.0 + 1 mM EDTA (Sigma-Aldrich, EDS-1 KG)), 0.5% v:v Tween 20 (VWR, 97,062–332), pH 9.0, and pressure cooked for 20 min at maximum pressure, then allowed to cool to RT for 1 h. Slides were then rinsed in wash buffer (1X TBS [50 mM Tris-Cl, pH 7.5 + 150 mM NaCl], 0.1% v:v Tween 20) and endogenous peroxidase activity was quenched in a solution of 3% H_2O_2 (in methanol) for 15 min, followed by 3 changes in wash buffer for 5 min each. Next, slides were incubated with blocking buffer (10% v:v donkey serum [Jackson Immunoresearch, 017–000-121] in wash buffer) for 20 min and rinsed in wash buffer. One hundred μL of PEX26 antibody (Novus Biologicals, NBP1-32,743) at 1:500 dilution was then added over of each tissue and incubated for 1 h at RT, then rinsed in 3 changes of wash buffer for 5 min each change. Two drops of HRP conjugate (Agilent Technologies, K400211-2) were added overtop each tissue for 30 min and washed in 4 changes of wash buffer for 5 min each change. 100 μL of DAB solution (Vector Laboratories, SK-4105) was added to each slide for 2 min and 30 s and immediately rinsed in 4 changes of wash buffer for 5 min each change, then rinsed in ddH_2O for 5 min. Tissues were then counterstained in filtered hematoxylin for 1 min, dipped in bluing buffer (37 mM NH_4OH) 10 times, and rinsed for 5 min in tap water. Next, tissues were dehydrated in 95% EtOH for 2 min, 100% EtOH for 1 min (repeated twice), and xylene for 30 s (repeated 3 times). Slides were covered with a thin layer of Permount mounting medium (Fisher Scientific, SP15-500) and a coverslip was placed on top.

Immunohistochemistry analysis

Images of stained tissues were taken using a Ziess Axioscan brightfield camera (20X objective). The mean DAB stain intensity per cell was obtained using QuPath v0.2.0-m4 software with the following method. Using the brightfield-DAB setting, a region of interest visually containing low, medium and high DAB staining was selected and stain vectors were estimating using automatic program settings. Using these settings, cells were then detected under the hematoxylin OD settings, with a requested pixel size 0.5 µm, background radius 10 µm, sigma 2 µm, threshold 0.05, and cell expansion 10 µm. From these settings positive cell detection was performed on each image, with fat cells excluded from analysis. The "cell: DAB OD mean" value was obtained for region of interest and the percent of cells ≥ 0.2 (versus the total cell number) was determined as the % DAB-positive. For multiple images per slide, the average was taken and plotted as a single value.

Statistical analysis

Student's t-tests (unpaired, two-tailed, 95% confidence interval) and One-Way ANOVA (Tukey's post test) were applied for statistical tests presented in this manuscript, using GraphPad Prism Version 9.0.0 unless otherwise stated.

Acknowledgments

We thank the Flow Cytometry and Animal Core Facilities of the Lady Davis Institute for their support. We are grateful to Dr. Chantal Autexier, Dr. Michael Witcher, Dr. Nathalie Johnson, and Carly Kraus for helpful discussions, as well as Christian Young for technical expertise. Electron Microscopy was conducted by the McGill Facility for Electron Microscopy Research (Jeannie Mui and S. Kelly Sears).

Disclosure statement

No potential conflict of interest was reported by the author(s).

Funding

This work was supported by the Canadian Cancer Society [703811]; Canadian Institutes of Health Research [PJT-156269]; Canadian Institutes of Health Research [MOP-142281]; Canadian Institutes of Health Research [PJT-162260]; Cancer Research Society [PIN 20239]; Fonds de Recherche du Québec - Santé [30253]; Fonds de Recherche du Québec - Santé [-]; Israel Cancer Research Fund [-]; Rossy Cancer Network [-]; Cole Foundation (CAN) [-].

ORCID

Fan Huang http://orcid.org/0000-0002-3850-5317
Joelle Rémy-Sarrazin http://orcid.org/0000-0002-3081-3307

References

[1] Galluzzi L, Pietrocola F, Bravo-San Pedro JM, et al. Autophagy in malignant transformation and cancer progression. EMBO J. 2015 Apr 1;34(7):856–880.
[2] Yu L, Chen Y, Tooze SA. Autophagy pathway: cellular and molecular mechanisms. Autophagy. 2018;14(2):207–215.
[3] Dupere-Richer D, Kinal M, Menasche V, et al. Vorinostat-induced autophagy switches from a death-promoting to a cytoprotective signal to drive acquired resistance. Cell Death Dis. 2013 Feb;7(4):e486.
[4] Mancias JD, Wang X, Gygi SP, et al. Quantitative proteomics identifies NCOA4 as the cargo receptor mediating ferritinophagy. Nature. 2014 May 1;509(7498):105–109.
[5] Dengjel J, Hoyer-Hansen M, Nielsen MO, et al. Identification of autophagosome-associated proteins and regulators by quantitative proteomic analysis and genetic screens. Mol Cell Proteomics. 2012 Mar;11(3):M111 014035.
[6] Khaminets A, Heinrich T, Mari M, et al. Regulation of endoplasmic reticulum turnover by selective autophagy. Nature. 2015 Jun 18;522(7556):354–358.
[7] Strzyz P. Foundations of ER-phagy regulation. Nat Rev Mol Cell Biol. 2020 May;21(5):251.
[8] Lemasters JJ. Selective mitochondrial autophagy, or mitophagy, as a targeted defense against oxidative stress, mitochondrial dysfunction, and aging. Rejuvenation Res. 2005 Spring;8(1):3–5.
[9] Zhang J, Tripathi DN, Jing J, et al. ATM functions at the peroxisome to induce pexophagy in response to ROS. Nat Cell Biol. 2015 Oct;17(10):1259–1269.
[10] Moser AB, Kreiter N, Bezman L, et al. Plasma very long chain fatty acids in 3,000 peroxisome disease patients and 29,000 controls. Ann Neurol. 1999 Jan;45(1):100–110.
[11] Ferdinandusse S, Denis S, Faust PL, et al. Bile acids: the role of peroxisomes. J Lipid Res. 2009 Nov;50(11):2139–2147.
[12] Wanders RJ, Vreken P, Ferdinandusse S, et al. Peroxisomal fatty acid alpha- and beta-oxidation in humans: enzymology, peroxisomal metabolite transporters and peroxisomal diseases. Biochem Soc Trans. 2001 May;29(Pt 2):250–267.
[13] Braverman NE, Moser AB. Functions of plasmalogen lipids in health and disease. Biochim Biophys Acta. 2012 Sep;1822 (9):1442–1452.
[14] DeBerardinis RJ, Chandel NS. Fundamentals of cancer metabolism. Sci Adv. 2016 May;2(5):e1600200.
[15] Matsumoto N, Tamura S, Fujiki Y. The pathogenic peroxin Pex26p recruits the Pex1p-Pex6p AAA ATPase complexes to peroxisomes. Nat Cell Biol. 2003 May;5(5):454–460.
[16] Argyriou C, D'Agostino MD, Braverman N. Peroxisome biogenesis disorders. Trans Sci Rare Dis. 2016 Nov 7;1(2):111–144.
[17] Law KB, Bronte-Tinkew D, Di Pietro E, et al. The peroxisomal AAA ATPase complex prevents pexophagy and development of peroxisome biogenesis disorders. Autophagy. 2017 May 4;13 (5):868–884.
[18] Dahabieh MS, Ha Z, Di Pietro E, et al. Peroxisomes protect lymphoma cells from HDAC inhibitor-mediated apoptosis. Cell Death Differ. 2017 Nov;24(11):1912–1924.
[19] Dunn WA Jr., Cregg JM, Kiel JA, et al. Pexophagy: the selective autophagy of peroxisomes. Autophagy. 2005 Jul;1(2):75–83.
[20] Iwata J, Ezaki J, Komatsu M, et al. Excess peroxisomes are degraded by autophagic machinery in mammals. J Biol Chem. 2006 Feb 17;281(7):4035–4041.
[21] Subramani S. A mammalian pexophagy target. Nat Cell Biol. 2015 Nov;17(11):1371–1373.
[22] Gao W, Kang JH, Liao Y, et al. Biochemical isolation and characterization of the tubulovesicular LC3-positive autophagosomal compartment. J Biol Chem. 2010 Jan 8;285 (2):1371–1383.
[23] Cox J, Hein MY, Luber CA, et al. Accurate proteome-wide label-free quantification by delayed normalization and maximal peptide ratio extraction, termed MaxLFQ. Mol Cell Proteomics. 2014 Sep;13(9):2513–2526.
[24] Gallinari P, Di Marco S, Jones P, et al. HDACs, histone deacetylation and gene transcription: from molecular biology to cancer therapeutics. Cell Res. 2007 Mar;17(3):195–211.
[25] Zhang J, Ng S, Wang J, et al. Histone deacetylase inhibitors induce autophagy through FOXO1-dependent pathways. Autophagy. 2015 Apr 3;11(4):629–642.

[26] Till A, Lakhani R, Burnett SF, et al. Pexophagy: the selective degradation of peroxisomes. Int J Cell Biol. 2012;2012:512721.
[27] Deosaran E, Larsen KB, Hua R, et al. NBR1 acts as an autophagy receptor for peroxisomes. J Cell Sci. 2013 Feb 15;126(Pt 4):939–952.
[28] Walter KM, Schonenberger MJ, Trotzmuller M, et al. Hif-2alpha promotes degradation of mammalian peroxisomes by selective autophagy. Cell Metab. 2014 Nov 4;20(5):882–897.
[29] Nuttall JM, Motley AM, Hettema EH. Deficiency of the exportomer components Pex1, Pex6, and Pex15 causes enhanced pexophagy in Saccharomyces cerevisiae. Autophagy. 2014 May;10(5):835–845.
[30] Mahalingam SS, Shukla N, Farre JC, et al. Balancing the opposing principles that govern peroxisome homeostasis. Trends Biochem Sci. 2020 Oct 9;46:200–212.
[31] Farkas T, Daugaard M, Jaattela M. Identification of small molecule inhibitors of phosphatidylinositol 3-kinase and autophagy. J Biol Chem. 2011 Nov 11;286(45):38904–38912.
[32] Golding SE, Rosenberg E, Valerie N, et al. Improved ATM kinase inhibitor KU-60019 radiosensitizes glioma cells, compromises insulin, AKT and ERK prosurvival signaling, and inhibits migration and invasion. Mol Cancer Ther. 2009 Oct;8(10):2894–2902.
[33] Lee JN, Dutta RK, Maharjan Y, et al. Catalase inhibition induces pexophagy through ROS accumulation. Biochem Biophys Res Commun. 2018 Jun 27;501(3):696–702.
[34] Zhan Y, Dahabieh MS, Rajakumar A, et al. The role of eIF4E in response and acquired resistance to vemurafenib in melanoma. J Invest Dermatol. 2015 May;135(5):1368–1376.
[35] Su F, Bradley WD, Wang Q, et al. Resistance to selective BRAF inhibition can be mediated by modest upstream pathway activation. Cancer Res. 2012 Feb 15;72(4):969–978.
[36] Larson MH, Gilbert LA, Wang X, et al. CRISPR interference (CRISPRi) for sequence-specific control of gene expression. Nat Protoc. 2013 Nov;8(11):2180–2196.
[37] Wiemer EA, Wenzel T, Deerinck TJ, et al. Visualization of the peroxisomal compartment in living mammalian cells: dynamic behavior and association with microtubules. J Cell Biol. 1997 Jan 13;136(1):71–80.
[38] Poulos A, Beckman K, Johnson DW, et al. Very long-chain fatty acids in peroxisomal disease. Adv Exp Med Biol. 1992;318:331–340.
[39] Wang W, Xia ZJ, Farre JC, et al. TRIM37, a novel E3 ligase for PEX5-mediated peroxisomal matrix protein import. J Cell Biol. 2017 Sep 4;216(9):2843–2858.
[40] Tugwood JD, Issemann I, Anderson RG, et al. The mouse peroxisome proliferator activated receptor recognizes a response element in the 5′ flanking sequence of the rat acyl CoA oxidase gene. EMBO J. 1992 Feb;11(2):433–439.
[41] Tsukamoto T, Yokota S, Fujiki Y. Isolation and characterization of Chinese hamster ovary cell mutants defective in assembly of peroxisomes. J Cell Biol. 1990 Mar;110(3):651–660.
[42] Ghaedi K, Honsho M, Shimozawa N, et al. PEX3 is the causal gene responsible for peroxisome membrane assembly-defective Zellweger syndrome of complementation group G. Am J Hum Genet. 2000 Oct;67(4):976–981.
[43] Das Thakur M, Salangsang F, Landman AS, et al. Modelling vemurafenib resistance in melanoma reveals a strategy to forestall drug resistance. Nature. 2013 Feb 14;494(7436):251–255.
[44] Xue G, Kohler R, Tang F, et al. mTORC1/autophagy-regulated MerTK in mutant BRAFV600 melanoma with acquired resistance to BRAF inhibition. Oncotarget. 2017 Sep 19;8(41):69204–69218.
[45] Flaherty KT, Puzanov I, Kim KB, et al. Inhibition of mutated, activated BRAF in metastatic melanoma. N Engl J Med. 2010 Aug 26;363(9):809–819.
[46] Villanueva J, Vultur A, Lee JT, et al. Acquired resistance to BRAF inhibitors mediated by a RAF kinase switch in melanoma can be overcome by cotargeting MEK and IGF-1R/PI3K. Cancer Cell. 2010 Dec 14;18(6):683–695.
[47] Nazarian R, Shi H, Wang Q, et al. Melanomas acquire resistance to B-RAF(V600E) inhibition by RTK or N-RAS upregulation. Nature. 2010 Dec 16;468(7326):973–977.
[48] Johannessen CM, Boehm JS, Kim SY, et al. COT drives resistance to RAF inhibition through MAP kinase pathway reactivation. Nature. 2010 Dec 16;468(7326):968–972.
[49] Aguirre-Gamboa R, Gomez-Rueda H, Martinez-Ledesma E, et al. SurvExpress: an online biomarker validation tool and database for cancer gene expression data using survival analysis. PLoS One. 2013;8(9):e74250.
[50] Petruccelli LA, Dupere-Richer D, Pettersson F, et al. Vorinostat induces reactive oxygen species and DNA damage in acute myeloid leukemia cells. PLoS One. 2011;6(6):e20987.
[51] Cho DH, Kim YS, Jo DS, et al. Pexophagy: molecular mechanisms and implications for health and diseases. Mol Cells. 2018 Jan 31;41(1):55–64.
[52] Dahabieh MS, Di Pietro E, Jangal M, et al. Peroxisomes and cancer: the role of a metabolic specialist in a disease of aberrant metabolism. Biochim Biophys Acta Rev Cancer. 2018 Aug;1870(1):103–121.
[53] Schrakamp G, Schalkwijk CG, Schutgens RB, et al. Plasmalogen biosynthesis in peroxisomal disorders: fatty alcohol versus alkylglycerol precursors. J Lipid Res. 1988 Mar;29(3):325–334.
[54] Benjamin DI, Cozzo A, Ji X, et al. Ether lipid generating enzyme AGPS alters the balance of structural and signaling lipids to fuel cancer pathogenicity. Proc Natl Acad Sci U S A. 2013 Sep 10;110(37):14912–14917.
[55] Bagattin A, Hugendubler L, Mueller E. Transcriptional coactivator PGC-1alpha promotes peroxisomal remodeling and biogenesis. Proc Natl Acad Sci U S A. 2010 Nov 23;107(47):20376–20381.
[56] Sharabi K, Lin H, Tavares CDJ, et al. Selective chemical inhibition of PGC-1alpha gluconeogenic activity ameliorates type 2 diabetes. Cell. 2017 Mar 23;169(1):148–160 e15.
[57] Long J, Zhang CJ, Zhu N, et al. Lipid metabolism and carcinogenesis, cancer development. Am J Cancer Res. 2018;8(5):778–791.
[58] Luo X, Cheng C, Tan Z, et al. Emerging roles of lipid metabolism in cancer metastasis. Mol Cancer. 2017 Apr 11;16(1):76.
[59] Lodhi IJ, Semenkovich CF. Peroxisomes: a nexus for lipid metabolism and cellular signaling. Cell Metab. 2014 Mar 4;19(3):380–392.
[60] Drissi R, Dubois ML, Douziech M, et al. Quantitative proteomics reveals dynamic interactions of the Minichromosome Maintenance Complex (MCM) in the cellular response to etoposide induced DNA damage. Mol Cell Proteomics. 2015 Jul;14(7):2002–2013.
[61] Gilbert LA, Larson MH, Morsut L, et al. CRISPR-mediated modular RNA-guided regulation of transcription in eukaryotes. Cell. 2013 Jul 18;154(2):442–451.
[62] Horlbeck MA, Gilbert LA, Villalta JE, et al. Compact and highly active next-generation libraries for CRISPR-mediated gene repression and activation. Elife. 2016 Sep 23;5. DOI:10.7554/eLife.19760